







Gemini NIFS survey of feeding and feedback processes in nearby active galaxies – VI. Stellar populations

Rogério Riffel ¹★, Luis G. Dahmer-Hahn,^{2,3} Rogemar A. Riffel ⁴, Thaisa Storchi-Bergmann,¹
Natacha Z. Dametto,⁵ Richard Davies ⁶, Leonard Burtscher,⁷ Marina Bianchin,⁴
Daniel Ruschel-Dutra ⁸, Claudio Ricci ^{9,10} and David J. Rosario ¹¹

¹Departamento de Astronomia, Instituto de Física, Universidade Federal do Rio Grande do Sul, CP 15051, 91501-970 Porto Alegre, RS, Brazil

²Shanghai Astronomical Observatory, Chinese Academy of Sciences, 80 Nandan Road, Shanghai 200030, China

³Laboratório Nacional de Astrofísica/MCTIC, Rua dos Estados Unidos, 154 Bairro das Nações, Itajubá, MG, 37504-364, Brazil

⁴Departamento de Física, Centro de Ciências Naturais e Exatas, Universidade Federal de Santa Maria, 97105-900 Santa Maria, RS, Brazil

⁵Centro de Astronomía (CITEVA), Universidad de Antofagasta, Avenida Angamos 601, Antofagasta, Chile

⁶Max-Planck-Institut für Extraterrestrische Physik, Postfach 1312, D-85741 Garching, Germany

⁷Leiden Observatory, PO Box 9513, NL-2300 RA Leiden, the Netherlands

⁸Departamento de Física, Universidade Federal de Santa Catarina, PO Box 476, 88040-900 Florianópolis, SC, Brazil

⁹Núcleo de Astronomía de la Facultad de Ingeniería, Universidad Diego Portales, Av. Ejército Libertador 441, Santiago, Chile

¹⁰Kavli Institute for Astronomy and Astrophysics, Peking University, Beijing 100871, China

¹¹School of Mathematics, Statistics and Physics, Newcastle University, Newcastle upon Tyne NE1 7RU, UK

Accepted 2022 March 14. Received 2022 March 2; in original form 2021 December 12

ABSTRACT

We use Gemini Near-Infrared Integral Field Spectrograph (NIFS) adaptive optics assisted data cubes to map the stellar population of the inner few hundred parsec of a sample of 18 nearby Seyfert galaxies. The near-infrared light is dominated by the contribution of young to intermediate-age stellar populations, with light-weighted mean ages $\langle t \rangle_L \lesssim 1.5$ Gyr. Hot dust (HD) emission is centrally peaked (in the unresolved nucleus), but it is also needed to reproduce the continuum beyond the nucleus in nearly half of the sample. We have analysed the stellar population properties of the nuclear region and their relation with more global properties of the galaxies. We find a correlation between the X-ray luminosity and the contributions from the HD, featureless continuum (FC), and reddening A_V . We attribute these correlations to the fact that all these properties are linked to the mass accretion rate to the active galactic nuclei (AGNs). We also find a correlation of the bolometric luminosity $\log(L_{\text{Bol,obs}})$ with the mass-weighted mean age of the stellar population, interpreted as due a delay between the formation of new stars and the triggering/feeding of the AGN. The gas reaching the supermassive black hole is probably originated from mass loss from the already somewhat evolved intermediate-age stellar population ($\langle t \rangle_L \lesssim 1.5$ Gyr). In summary, our results show that there is a significant fraction of young to intermediate-age stellar populations in the inner few 100 pc of active galaxies, suggesting that this region is facing a rejuvenation process in which the AGN, once triggered, precludes further star formation, in the sense that it can be associated with the lack of new star formation in the nuclear region.

Key words: galaxies: active – galaxies: evolution – galaxies: stellar content.

1 INTRODUCTION

Since the pioneering studies linking the mass of supermassive black holes (SMBHs) with the velocity dispersion of their host galaxies bulges it has become accepted that the products of active galactic nuclei (AGNs) accretion and star formation are related (e.g. Magorrian et al. 1998; Ferrarese & Merritt 2000; Gebhardt et al. 2000). It is also accepted that nuclear star formation and AGN can coexist in the inner region of galaxies, suggesting that the growth of SMBH (by gas accretion) and galaxies (by star formation) is coupled (see Heckman & Best 2014; Madau & Dickinson 2014, for a review). In the modern view of galaxy evolution, it is well established that

AGN feedback plays a fundamental role by impacting (quenching, suppressing, or triggering) star formation from nuclear to galactic scales (e.g. Di Matteo, Springel & Hernquist 2005; Hopkins & Elvis 2010; Harrison 2017; Storchi-Bergmann & Schnorr-Müller 2019; Ellison et al. 2021; Riffel et al. 2021a).

Theoretical studies and simulations of gas inflows around galactic nuclei lead to episodes of star formation in the nuclear region ($r \lesssim 100$ pc; Kormendy & Ho 2013, for example). In this sense, one of the most popular processes invoked to regulate star formation is the AGN feedback (Terrazas et al. 2020, and references therein). The accretion of matter into an SMBH, which leads to the triggering of an AGN, can in fact inject enough energy into the galaxy affecting its star formation by heating (or removing) the gas (e.g. Granato et al. 2004; Fabian 2012; Zubovas et al. 2013; King & Pounds 2015; Zubovas & Bourne 2017; Trussler et al. 2020) or, as suggested in

* E-mail: riffel@ufrgs.br

other studies, these outflows and jets, can in some cases (depending on the AGN luminosity), compress the galactic gas, and therefore act as a catalyzer, boosting the star formation (e.g. Rees 1989; Hopkins 2012; Nayakshin & Zubovas 2012; Zubovas et al. 2013; Bieri et al. 2016; Zubovas & Bourne 2017) and even form stars inside the outflow (e.g. Ishibashi & Fabian 2012; Zubovas et al. 2013; El-Badry et al. 2016; Wang & Loeb 2018, for observational examples, see Maiolino et al. 2017; Gallagher et al. 2019).

It is also well established that cosmological simulations performed without the inclusion of feedback effects are not able to reproduce the low- and high-luminosity ends of the galaxy luminosity function (e.g. Springel et al. 2005; Vogelsberger et al. 2014; Crain et al. 2015), and underestimate the ages of the stars of the most massive galaxies when compared with observations (Croton et al. 2006). These results clearly show that an effective feedback is required to reproduce the galaxy properties, but simulations can only provide limited insight on the nature and source of the feedback processes (AGN or supernova dominated; Schaye et al. 2015). This is because the observations are limited and do not provide strong enough constraints to be used in the modelling. In particular, in the case of AGN hosts it is necessary to robustly quantify the star formation history (SFH) in the inner region of AGN hosts to see if star formation is boosted or quenched (Riffel et al. 2021a).

Observations have clearly shown that nuclear star formation is common in AGNs (e.g. Terlevich, Diaz & Terlevich 1990; Storch-Bergmann et al. 2001, 2012; Cid Fernandes et al. 2004; Riffel et al. 2007, 2009, 2016, 2021a; Esquej et al. 2014; Ruschel-Dutra et al. 2017; Hennig et al. 2018; Mallmann et al. 2018; Burtscher et al. 2021). Since AGN activity is most likely intermittent on time-scales ~ 0.1 – 1 Myr (Novak, Ostriker & Ciotti 2011; Schawinski et al. 2015), while the time-scale of star formation in the host galaxy is much longer (~ 100 Myr; Hickox et al. 2014; Burtscher et al. 2021), it is very difficult to compare the AGN life cycle with nuclear starbursts ages (which have an uncertainty that may be larger than the time to trigger AGN activity). Therefore, these types of studies are rare and their results inconclusive.

The triggering mechanism of nuclear activity is still unclear (see Alexander & Hickox 2012; Storch-Bergmann & Schnorr-Müller 2019, for a review). Over the years many mechanisms were discussed as being the drivers (or not) of AGN activity, for example: galactic environment (e.g. Mauduit & Mamon 2007; Davies et al. 2017; Marshall et al. 2018), mergers (e.g. Villforth et al. 2014; Goulding et al. 2018; Pan et al. 2019; Gao et al. 2020; Marian et al. 2020, and references therein), bar instabilities (e.g. Knapen, Shlosman & Peletier 2000), accretion of gas clouds (e.g. Maccagni et al. 2014), and dust lanes (Lopes et al. 2007; Prieto et al. 2019).

In addition, a dusty torus, rich in molecular gas, is located in the inner parts of the host galaxy (e.g. Antonucci 1993; Rodríguez-Ardila et al. 2004; Rodríguez-Ardila, Riffel & Pastoriza 2005; Riffel et al. 2013a, 2021b; Ramos-Almeida & Ricci 2017; García-Burillo et al. 2019, 2021; Bewketu Belete et al. 2021). Such a huge gas reservoir could be responsible for nuclear activity (Reichard et al. 2009), and since the most important ingredient for star formation is the availability of a large amount of cold gas (Kennicutt & Evans 2012), the same gas fuelling the AGN could be used to form stars. However, there is no consensus on whether AGN fuelling occurs at the same time as star formation (Kawakatu & Wada 2008), follows it during a post-starburst phase (Davies et al. 2007; Riffel et al. 2009) or there is a lack of any association with recent star formation (Sarzi et al. 2007).

Literature results trying to connect the AGN and star formation are controversial. Studies suggest that the fraction of young stars in

the vicinity of AGN are usually related with the luminosity of the AGN, with the most luminous AGNs presenting larger fractions of young stellar populations (e.g. Riffel et al. 2009; Ellison et al. 2016; Ruschel-Dutra et al. 2017; Zubovas & Bourne 2017; Mallmann et al. 2018). Less efficient processes may be sufficient to supply lower accretion rates. Davies et al. (2007), for example, have shown that the age of the starburst is associated with the AGN luminosity. On the other hand in Burtscher et al. (2021) no relation of the X-ray luminosity with the fraction of young stellar population was found. Indeed, many of the confusing or inconclusive results about local AGN may be attributable to the luminosity being a ‘third parameter’: previous analyses of local AGN have typically been performed for objects with low luminosities (e.g. Davies et al. 2015).

It is, then, fundamental to this debate to investigate if there is an association between star formation and nuclear activity, by mapping the stellar population properties in the inner few tens of parsec around AGNs over a wide range of AGN luminosities and in a wavelength region sensitive to the AGN featureless components [accretion disc and hot dust (HD) emission] and the stellar population at the same time. The ideal spectral region for this is the near-infrared (NIR = ~ 0.8 – 2.4 μm) where the AGN featureless continuum (FC), the HD, and the stellar population components (SPCs) can be fitted together and disentangled (Riffel et al. 2009, 2011b).

Here we map the SPCs in the inner few hundred parsec of a volume limited, X-ray luminosity selected, and adaptive optics (AO) assisted observed sample of AGNs, the *Gemini Near-Infrared Integral Field Spectrograph (NIFS) survey of feeding and feedback processes in nearby active galaxies* (Riffel et al. 2017, 2018, 2021b; Schönell et al. 2017; Bianchin et al. 2022). This paper is structured as follows. In Section 2, we present the sample, observations, and data reduction. The stellar population synthesis procedures are presented in Section 3. Results are presented in Section 4. The discussion is made in Section 5, while the conclusions are presented in Section 6. We have adopted $H_0 = 69.32$ $\text{km s}^{-1} \text{Mpc}^{-1}$ from the 9-year *Wilkinson Microwave Anisotropy Probe (WMAP)* observations (Hinshaw et al. 2013) available in *ASTROPY* package (Astropy Collaboration et al. 2018).

2 SAMPLE AND OBSERVATIONS

2.1 The sample

The present sample is composed of the galaxies in the Gemini NIFS survey of feeding and feedback processes in nearby active galaxies (Riffel et al. 2017, 2018) that have observations in the *J* and *K* (or *K_s*) bands. In short, the sample was selected using the *Swift*-Burst Alert Telescope (BAT) 60-month catalogue (Ajello et al. 2012), and selected nearby galaxies with 14–195 keV luminosities $L_X \geq 10^{41.5}$ erg s^{-1} . Such selection guarantees a high completeness, since hard X-ray selected samples are not significantly biased against obscuration, up to column density of $N_H \simeq 10^{24}$ cm^{-2} (see fig. 1 of Ricci et al. 2015). As additional criteria, the object must be accessible for Gemini NIFS ($-30^\circ < \delta < 73^\circ$), and either its nucleus must be bright/pointy enough to guide the adaptive optics system during the observations or there must be a natural guide star available in the field for the same purpose. Finally, we only have included in the sample galaxies already previously observed in the optical and with extended [O III] $\lambda 5007$ emission available in the literature. This sample was completed with data already observed by the AGN Integral Field Spectroscopy (AGNIFS) team in other projects. For additional details see Riffel et al. (2018). Our final sample is composed of 18 local Universe ($0.00303 \leq z \leq 0.02213$; $13.10 \leq d \leq 95.71$ Mpc) sources,

Table 1. Sample properties.

Galaxy (1)	z (2)	d (3)	Nuc. act. (4)	Hub. type (5)	L_X^{obs} (6)	L_X^{int} (7)	$L_{\text{Bol}}^{\text{obs}}$ (8)	$L_{\text{Bol}}^{\text{int}}$ (9)	σ_* (10)	M_\bullet (11)	L_{Edd} (12)	λ_{obs} (13)	λ_{int} (14)	$M(\text{H}_2)$ (15)	$M(\text{H II})$ (16)
NGC 788	0.01365	59.03	Sy2	SA0/a?(s)	42.13	43.02	43.33	44.42	187 ± 4	8.04 ± 0.07	46.14	1.55E-03	1.91E-02	12.81 ± 0.46	19.54 ± 0.6
NGC 1052†	0.00446	19.29	Sy2	E4	41.36	41.52	42.45	42.63	245 ± 4	8.44 ± 0.06	46.54	8.13E-05	1.23E-04	11.02 ± 1.14	5.67 ± 1.63
Mrk 79	0.02213	95.71	Sy1.5	SBb	42.93	43.10	44.30	44.52	130 ± 10	7.51 ± 0.21	45.61	4.90E-02	8.13E-02	52.9 ± 2.09	23.86 ± 2.49
NGC 1125	0.01128	48.78	Sy2	(R')SB(r)0/a?	41.06	42.76	42.10	44.10	118 ± 9	7.37 ± 0.21	45.47	4.27E-04	4.27E-02	21.26 ± 0.69	64.11 ± 0.83
NGC 1068†	0.00303	13.10	Sy2	(R)SA(rs)b	41.00	42.74	42.05	44.07	162 ± 5	7.83 ± 0.09	45.93	1.32E-04	1.38E-02	202.28 ± 2.19	191.95 ± 3.84
NGC 2110†	0.00739	31.96	Sy2	SAB0 ⁻	42.48	42.65	43.75	43.96	238 ± 5	8.40 ± 0.07	46.50	1.78E-03	2.88E-03	41.71 ± 0.84	16.75 ± 0.98
NGC 3227	0.00329	14.23	Sy1.5	SAB(s)a pec	41.95	41.95	43.12	43.13	130 ± 7	7.51 ± 0.14	45.61	3.24E-03	3.31E-03	52.11 ± 1.3	11.52 ± 1.23
NGC 3516	0.00871	37.67	Sy1.5	(R)SB0 ⁰ ?(s)	42.67	42.72	43.98	44.04	186 ± 3	8.03 ± 0.06	46.13	7.08E-03	8.13E-03	8.69 ± 2.19	1.97 ± 0.34
NGC 4151	0.00314	13.58	Sy1	SAB(rs)bc	42.02	42.27	43.20	43.50	97 ± 3	7.08 ± 0.07	45.18	1.05E-02	2.09E-02	36.89 ± 1.31	54.77 ± 1.54
NGC 4235	0.00757	32.74	Sy1	SA(s)a edge-on	41.56	41.56	42.66	42.66	183 ± 12	8.01 ± 0.20	46.11	3.55E-04	3.55E-04	3.98 ± 0.5	0.19 ± 0.07
NGC 5506	0.00609	26.34	Sy1.9	Sa pec edge-on	42.89	42.98	44.25	44.37	180 ± 20	7.99 ± 0.37	46.09	1.45E-02	1.91E-02	45.71 ± 0.72	174.09 ± 1.41
NGC 5548†	0.01673	72.35	Sy1	(R')SA0/a(s)	43.08	43.12	44.49	44.54	276 ± 22	8.61 ± 0.28	46.71	6.03E-03	6.76E-03	33.29 ± 5.54	32.06 ± 6.76
NGC 5899	0.00844	36.50	Sy2	SAB(rs)c	41.91	42.21	43.07	43.42	147 ± 9	7.69 ± 0.17	45.79	1.91E-03	4.27E-03	17.79 ± 0.8	6.58 ± 1.09
NGC 5929	0.00831	35.94	Sy2	Sab? pec	40.10	41.58	41.08	42.69	134 ± 5	7.55 ± 0.10	45.65	2.69E-05	1.10E-03	17.1 ± 0.9	11.4 ± 0.5
Mrk 607	0.00888	38.40	Sy2	Sa? edge-on	41.83	43.73	42.98	45.32	132 ± 4	7.53 ± 0.08	45.63	2.24E-03	4.90E-01	7.1 ± 0.41	11.3 ± 0.74
Mrk 766	0.01292	55.88	Sy1.5	(R')SB(s)a?	42.69	42.72	44.01	44.04	78 ± 6	6.76 ± 0.18	44.86	1.41E-01	1.51E-01	23.28 ± 1.95	112.21 ± 3.69
Mrk 1066†	0.01202	51.98	Sy2	(R)SB0 ⁺ (s)	40.72	42.63	41.74	43.94	103 ± 4	7.17 ± 0.09	45.27	2.95E-04	4.68E-02	57.33 ± 0.44	68.86 ± 0.73
Mrk 1157†	0.01517	65.61	Sy2	(R')SB0/a	40.29	42.87	41.28	44.22	92 ± 4	7.00 ± 0.10	45.10	1.51E-04	1.32E-01	9.80 ± 1.9	53.3 ± 1.3

Note. † – Stellar population studies previously published by the AGNIFS team. (1) Galaxy's name; (2) distance in Mpc; (3) redshift taken from the BAT AGN Spectroscopic Survey (BASS) Data Release 1 (DR1; Koss et al. 2017; Ricci et al. 2017; Oh et al. 2018, <http://www.bass-survey.com/>); (4) nuclear activity; (5) Hubble type as quoted in NASA/IPAC Extragalactic Database (NED); (6) logarithm of the observed hard X-ray luminosity (14–195 keV, in erg s^{-1}) from the BASS DR1, except for Mrk 1157, Mrk 1066, and NGC 5929 that are from Cardamone et al. (2007) and Mrk 607 that is from LaMassa et al. (2011); (7) logarithm of the intrinsic hard X-ray luminosity (14–195 keV, in erg s^{-1}) from the BASS DR1, except for Mrk 1157, Mrk 1066, NGC 5929, and Mrk 607 where we have calculated their values; (8) logarithm of the bolometric luminosity calculated using the observed hard X-ray luminosity (in erg s^{-1}); (9) logarithm of the bolometric luminosity calculated using the intrinsic hard X-ray luminosity (in erg s^{-1}); (10) σ (km s^{-1}) taken from Riffel et al. (2017) except for NGC 1068 (Storchi-Bergmann et al. 2012), NGC 4151 (Ho et al. 2009), NGC 1125 (Garcia-Rissmann et al. 2005), NGC 5506 (Oliva et al. 1999), and Mrk 79 (Greene & Ho 2006); (11) logarithm of the supermassive black hole (SMBH) mass in M_\odot computed using the M - σ relation from Caglar et al. (2020); (12) logarithm of the Eddington luminosity (Rybicki & Lightman 1979); (13) Eddington ratio computed with $L_{\text{Bol}}^{\text{obs}}$; (14) Eddington ratio computed with $L_{\text{Bol}}^{\text{int}}$; (15) H_2 mass (in $10 M_\odot$) in the inner 125 pc taken from Riffel et al. (2021a); (16) H II mass (in $10^4 M_\odot$) in the inner 125 pc taken from Riffel et al. (2021a).

listed in Table 1. It includes six galaxies with results on the stellar populations already published by the AGNIFS team (Riffel et al. 2010, 2011c; Storchi-Bergmann et al. 2012; Schönell et al. 2017; Dahmer-Hahn et al. 2019a,b; Diniz et al. 2019). These galaxies are identified with the † symbol after their names.

In order to compare the stellar population properties with more general ones, we have also collected or computed additional properties for the galaxies, as follows.

(i) Observed X-ray luminosities (2–10 keV) were taken from the BAT AGN Spectroscopic Survey (BASS) Data Release 1 (DR1; Koss et al. 2017; Ricci et al. 2017). The exceptions are Mrk 1157, Mrk 1066, and NGC 5929 that are from Cardamone, Moran & Kay (2007) and Mrk 607 from LaMassa et al. (2011).

(ii) Intrinsic X-ray luminosities were also collected from the BASS DR1, except for Mrk 1157, Mrk 1066, NGC 5929, and Mrk 607 where we have calculated their values as follows. For all sources we collected archival data, which include *XMM-Newton* (Mrk 607, Mrk 1066, and Mrk 1157), *Chandra* (NGC 5929), *Swift/BAT* (Mrk 1066), and *NuSTAR* (Mrk 607 and NGC 5929). The spectra were reduced and fitted following the same approach outlined in Ricci et al. (2017). We found that all objects are heavily obscured, with three of them (Mrk 607, Mrk 1066, and Mrk 1157) having Compton-thick ($N_{\text{H}} \geq 10^{24} \text{ cm}^{-2}$) column densities.

(iii) The bolometric luminosity was calculated using the observed X-ray luminosity together with the equation (Ichikawa et al. 2017)

$$\log L_{\text{bol}} = 0.0378(\log L_{2-10})^2 - 2.00 \log L_{2-10} + 60.5.$$

(iv) Stellar velocity dispersion (σ) was taken from Riffel et al. (2017) except for NGC 1068 (Storchi-Bergmann et al. 2012), NGC 4151 (Ho et al. 2009), NGC 1125 (Garcia-Rissmann et al. 2005), NGC 5506 (Oliva et al. 1999), and Mrk 79 (Greene & Ho 2006).

(v) The SMBH mass was computed using the M - σ relation from Caglar et al. (2020):

$$\log \left(\frac{M_\bullet}{M_\odot} \right) = (8.14 \pm 0.20) + (3.38 \pm 0.65) \log \left(\frac{\sigma_e}{200 \text{ km s}^{-1}} \right).$$

(vi) The Eddington luminosity (Rybicki & Lightman 1979):

$$L_{\text{Edd}} = 1.26 \times 10^{46} \text{ erg s}^{-1} \frac{M_\bullet}{10^8 M_\odot}.$$

(vii) Eddington ratio was obtained from L_{Bol} and calculated using the observed L_X ($\lambda_{\text{obs}} = L_{\text{Bol}}^{\text{obs}}/L_{\text{Edd}}$) and intrinsic X-ray luminosity ($\lambda_{\text{int}} = L_{\text{Bol}}^{\text{int}}/L_{\text{Edd}}$).

(viii) H_2 and H II masses in the inner 125 pc were taken from Riffel et al. (2021b).

2.2 Observations

The observations of our sample were done with the Gemini NIFS (McGregor et al. 2003). All observations were performed using the Gemini North adaptive optics system ALTitude conjugate Adaptive optics for the InfraRed (ALTAIR) from 2006 to 2018, except for NGC 1125 that was observed in the seeing limited mode (Riffel et al. 2018, 2021b). The observations followed an object–sky–object dither sequence, with sky observations made off-source since all targets are extended. Individual exposure times varied according to the target. The data comprise *J* and *K* (K_1)-band observations at angular resolutions in the range 0.12–0.20 arcsec, depending on the performance of the adaptive optics module. Additional details can be found in Riffel et al. (2018).

The angular resolution for each galaxy was derived from the full width at half-maximum (FWHM) of the flux distribution of the standard stars, corresponding to few tens of parsec at the distance of most galaxies as presented in Riffel et al. (2017, 2021b).

2.3 Data reduction

The data reduction followed the standard procedure and was performed using tasks that were specifically developed for NIFS data reduction, contained in the NIFS package, which is part of the GEMINI IRAF package, as well as generic IRAF tasks (Tody 1986, 1993). The procedures included the trimming of the images, flat-fielding, sky subtraction, wavelength, and s-distortion calibrations.

The telluric absorption corrections have been performed using the spectra of telluric A-type standard stars, observed just before/after the observation of each galaxy. They were also used to flux calibrate the spectra of the galaxies by interpolating a blackbody function to their spectra. Finally, data cubes were created for each individual exposure at an angular sampling of 0.15×0.15 arcsec² and combined in a final data cube for each galaxy. All data cubes cover the inner $\sim 3 \times 3$ arcsec², with exception of the data cube for NGC 4151 that covers the inner $\sim 3 \times 4$ arcsec², due to spatial dithering during the observations (Storchi-Bergmann et al. 2009, 2010) and for NGC 1068, covering the inner 5×5 arcsec² (Storchi-Bergmann et al. 2012; Barbosa et al. 2014; Riffel et al. 2014).

We followed the steps used in previous papers of the AGNIFS group (e.g. Riffel et al. 2011c; Storchi-Bergmann et al. 2012; Dahmer-Hahn et al. 2019a; Dametto et al. 2019; Diniz et al. 2019), since the different bands of our data were acquired during different nights. We have cross-calibrated the data cubes using cross-dispersed (XD) long-slit data presented by Riffel, Rodríguez-Ardila & Pastoriza (2006), Riffel et al. (2013b, 2015, 2019), and Mason et al. (2015) or unpublished XD spectra (Riffel et al., in preparation).

3 STELLAR POPULATION SYNTHESIS

The galaxies' integrated spectra are composed of several components, such as the underlying stellar (and gas) continuum and dust emission. In the case of active galaxies, besides the above, AGN torus and accretion disc components also need to be considered (Riffel et al. 2009; Burtscher et al. 2015). The stellar population synthesis consists of disentangling the per cent contribution of these components from the integrated spectrum.

It is worth mentioning that since there are a large number of parameters (e.g. age, metallicity, kinematics and reddening, and AGN components) to be fitted, many techniques have been employed over the years to disentangle the components of a galaxy spectrum (for a review see Walcher et al. 2011; Conroy 2013). Therefore, many fitting codes have been developed by different groups (e.g. Cid Fernandes et al. 2005; Ocvirk et al. 2006; Tojeiro et al. 2007; Koleva et al. 2009; Sánchez et al. 2016; Cappellari 2017; Gomes & Papaderos 2017; Wilkinson et al. 2017; Johnson et al. 2021) with their own priorities in mind (see Gomes & Papaderos 2017, for example). Naturally, comparisons among the different codes have also been presented, and they show that in general the codes do produce consistent results when fitting the same data with the same ingredients (e.g. Koleva et al. 2008; Dias et al. 2010; Goddard et al. 2017; Gomes & Papaderos 2017; Cid Fernandes 2018; Ge et al. 2018).

To perform the stellar population synthesis we applied STARLIGHT¹ (Cid Fernandes et al. 2004, 2005; Asari et al. 2007; Cid Fernandes 2018). The code fits the full underlying absorption and continuum in the observed spectra as a combination of different proportions of the base of elements, excluding emission lines and spurious data, mixing computational techniques originally developed for semi-empirical population synthesis with ingredients from evolutionary synthesis models (Cid Fernandes et al. 2004, 2005). In summary, the code fits an observed spectrum, O_λ , with a combination, in different proportions, of N_* simple stellar populations (SSPs). The visual extinction, A_V , is modelled by STARLIGHT as due to foreground dust. In the fits we use the Cardelli–Clayton–Mathis (CCM; Cardelli,

Clayton & Mathis 1989) extinction law. The modelled spectrum, M_λ , is obtained through the following equation:

$$M_\lambda = M_{\lambda_0} \sum_{j=1}^{N_*} x_j b_{j,\lambda} r_\lambda \otimes G(v_*, \sigma_*), \quad (1)$$

where x_j is the population vector, $b_{j,\lambda}$ is the j th base element, r_λ is the reddening factor of the j th component normalized at λ_0 , the reddening term is represented by $r_\lambda = 10^{-0.4(A_\lambda - A_{\lambda_0})}$, M_{λ_0} is the synthetic flux at the normalization wavelength (we have used $\lambda_{\text{norm}} = 21\,100$ Å in the rest frame). The convolution operator is \otimes and $G(v_*, \sigma_*)$ is the Gaussian distribution used to model the line-of-sight velocity distributions of the stars, which is centred at velocity v_* with dispersion σ_* . The final fit is carried out through a chi-square minimization, as follows:

$$\chi^2 = \sum_{\lambda} [(O_\lambda - M_\lambda) w_\lambda]^2, \quad (2)$$

where emission lines and spurious features are excluded from the fit by fixing $w_\lambda = 0$ at the corresponding wavelengths.

In this paper, we have followed Riffel et al. (2009, 2011b) and used as SSP the evolutionary population synthesis (EPS) models of Maraston (2005). These models are able to foresee characteristic near-infrared (NIR) absorption features (e.g. Riffel et al. 2007, 2015) and to produce consistent results when compared with properties of the emission line gas in star-forming regions of galaxies (Dametto et al. 2019). The base of elements comprises SSPs with four metallicities ($Z = 0.02, 0.5, 1, \text{ and } 2 Z_\odot$) and 12 ages ($t = 0.01, 0.03, 0.05, 0.1, 0.2, 0.5, 0.7, 1, 2, 5, 9, \text{ and } 13$ Gyr). To account for the accretion disc FC we have used a power law of the form $F_\lambda \propto \lambda^{-0.5}$ (e.g. Koski 1978; Cid Fernandes et al. 2005). In order to properly account for the HD emission component, eight Planck distributions (blackbody, BB), with temperature ranging from 700 to 1400 K, in steps of 100 K, were included in the fits. The lower limit was chosen because lower temperatures are hard to detect in this spectral range (Riffel et al. 2009) and the upper limit is very close to the sublimation temperature of the dust grains (e.g. Barvainis 1987; Granato & Danese 1994). For more details on the effects of these components in the NIR spectra and on the definition of our base of elements, see Riffel et al. (2009). The components used in the fits are shown in Fig. 1.

4 RESULTS

Since STARLIGHT is not designed to deal with data cubes, we have used the in-house MEGACUBE tool (Mallmann et al. 2018) as a front end for STARLIGHT fits and to produce maps for the derived quantities. Therefore each single spaxel was corrected for galactic extinction using the Schlegel, Finkbeiner & Davis (1998) dust maps and redshift corrected using the values listed in Table 1. An example of individual spectrum fits can be seen in Fig. 2.

To take into account the noise effects on the data that wash away differences between similar spectral components, as well as the age–metallicity degeneracy² (e.g. Worthey et al. 1994), we have followed Cid Fernandes et al. (2005) and Riffel et al. (2009) and we have defined condensed population vectors and have produced maps and

¹This choice was made mainly to produce self-consistent results with the previous studies done by our team, allowing for easier comparisons of the results.

²The difference between two spectrally similar populations may be in the noise level of the data; by binning them in a condensed population vector, we are left with a coarser but more robust fraction for each age bin. For a detailed test see section 3.2 of Cid Fernandes et al. (2004).

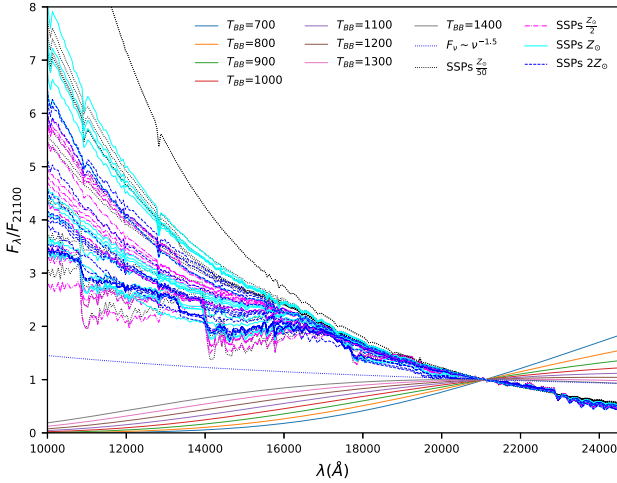


Figure 1. The base of elements comprises simple stellar populations (SSPs) with four metallicities ($Z = 0.02, 0.5, 1,$ and $2 Z_{\odot}$) and 12 ages ($t = 0.01, 0.03, 0.05, 0.1, 0.2, 0.5, 0.7, 1, 2, 5, 9,$ and 13 Gyr). The accretion disc (FC) is described as a power law of the form $F_{\lambda} \propto \lambda^{-0.5}$. HD emission components are described as eight Planck distributions (blackbody, BB), with temperature ranging from 700 to 1400 K, in steps of 100 K. The identification of the components is on the labels. For details see text.

radial profiles for different properties, for each one of the galaxies, as follows:

- xy : sum of the per cent contribution of SSPs with ages $t \leq 50$ Myr;
- xyo : sum of the per cent contribution of SSPs with ages in the range $100 \leq t \leq 200$ Myr;
- xiy : sum of the per cent contribution of SSPs with ages in the range $500 \leq t \leq 700$ Myr;
- xio : sum of the per cent contribution SSPs with ages in the range $1 \leq t \leq 2$ Gyr;
- xo : sum of the per cent contribution $5 \leq t \leq 13$ Gyr;
- HD: sum of the per cent contribution of all Planck function components;
- FC: is the featureless per cent contribution;
- $\langle t \rangle_L$: is the light-weighted mean age, which is defined as follows (Cid Fernandes et al. 2005):

$$\langle \log t_{\star} \rangle_L = \sum_{j=1}^{N_{\star}} x_j \log t_j. \quad (3)$$

Note that all these values are in light fractions and are limited by the elements included in the base.

An example of the maps is shown in Fig. 3 (the remaining maps are in the supplementary material). The red cross marks the peak of the continuum at the normalization point. In the same plot, we show radial profiles for these properties. The profiles shown in Fig. 3 were built using the MEGACUBE tool (Mallmann et al. 2018) and we used the standard 30 equally spaced (in azimuthal angle) radial profiles. These profiles, in the galaxy plane, have been limited to angular distances from the major axis of $\theta_{\max} = \tan^{-1}(b/a)$ degrees, where a and b are, respectively, the mean values of the semimajor and semiminor axis that were derived using the PHOTUTILS.ISOPHOTE ELLIPSE ASTROPY affiliated package (Bradley et al. 2019). The solid line represents the mean value and the shaded region is its standard deviation. The dotted vertical line is the point spread function (PSF) of the FWHM taken from Riffel et al. (2017, 2021b). To remove possible spurious data, not removed in the fits, we have recomputed

the standard STARLIGHT Adevs value as follows:

$$\text{Adevs} = \frac{100}{N_1^{\text{eff}}} \sum \frac{|F_{\text{obs}} - F_{\text{syn}}|}{F_{\text{syn}}}, \quad (4)$$

where N_1^{eff} is the number of points used in the fits, while, F_{obs} and F_{syn} are the observed and synthesized fluxes, respectively. We have identified all points with $\text{Adevs} > 10$ (red lines) and $\text{Adevs} > 20$ (white lines). It is clear that almost all the spaxels in all analysed sources have $\text{Adevs} \leq 10$. For the radial profiles, however, we used all spaxels, and the loss of quality on the fits is observed as a larger scatter around the mean values for large radii.³

For completeness, we have refitted the stellar populations of the six galaxies already studied by the AGNIFS team, and we present the corresponding maps and profiles as supplementary material.

4.1 Individual results

NGC 788. The light of this galaxy shows an important contribution of the two younger (xy and xyo) components with a maximum value of ~ 40 per cent. The radial profiles show that these two components only show up in the outer parts of the field of view (FoV). It is, however, worth mentioning that there is a ‘stripe’ on the east side that can be due to an instrumental fingerprint (not completely removed in the data reduction process), therefore this should just be taken as a trend. It is clear from these maps that the light of the central region of this galaxy is dominated by stars with ages in the range $500 \leq t \leq 700$ Myr (xiy) with contributions > 40 per cent over the FoV. A fraction of ~ 25 per cent of older stars (xio and xo SPC) are detected throughout the whole FoV. HD emission contributes 35 per cent of the nuclear emission of this source, while no FC is required. The mean age shows a negative profile with the central region having older stellar populations than the outer parts.

NGC 1052. This source is dominated by intermediate- and old-age stellar populations. A very tiny fraction of FC is found in the unresolved nucleus. The stellar content of this galaxy is discussed in detail in Dahmer-Hahn et al. (2019a,b).

Mrk 79. A clear ring-like structure is observed in the xy and xyo SPC, with a fraction reaching 50 per cent for the xyo population. Negligible contributions of the intermediate-age components are observed, with a smoother central distribution of older stars (xo) surrounded by the xyo ring-like ($r \geq 300$ pc) SPC. HD emission is observed over the entire FoV showing a maximum in the nuclear region. A FC emission of ~ 40 per cent is detected in the nuclear region. In the mean age map we see that the central region of this galaxy is dominated by a 2 Gyr population.

NGC 1125. This galaxy presents a complex SFH. Locations 100 pc from the centre towards the north-west (NW) are dominated by a xy SPC, reaching values up to 50 per cent. A ring-like structure is observed in the xyo map starting at ~ 100 pc from the centre with a fraction of ~ 25 per cent. This ring structure surrounds a ring of intermediate-age stars (xiy), which dominates the light in the central region of this galaxy. Fractions of ~ 25 per cent for the two older components are also observed, being located in regions from the centre towards the north. A vertical stripe can be seen in the east direction in this xo component (and as already mentioned before for other galaxies, it can be due to a residual instrumental fingerprint). HD emission is seen in the unresolved centre ($r \leq 100$ pc) of the

³The radial profiles have been obtained by averaging the individual (deprojected) profiles obtained along each one of the yellow lines (in both directions) in the top panel of the figures.

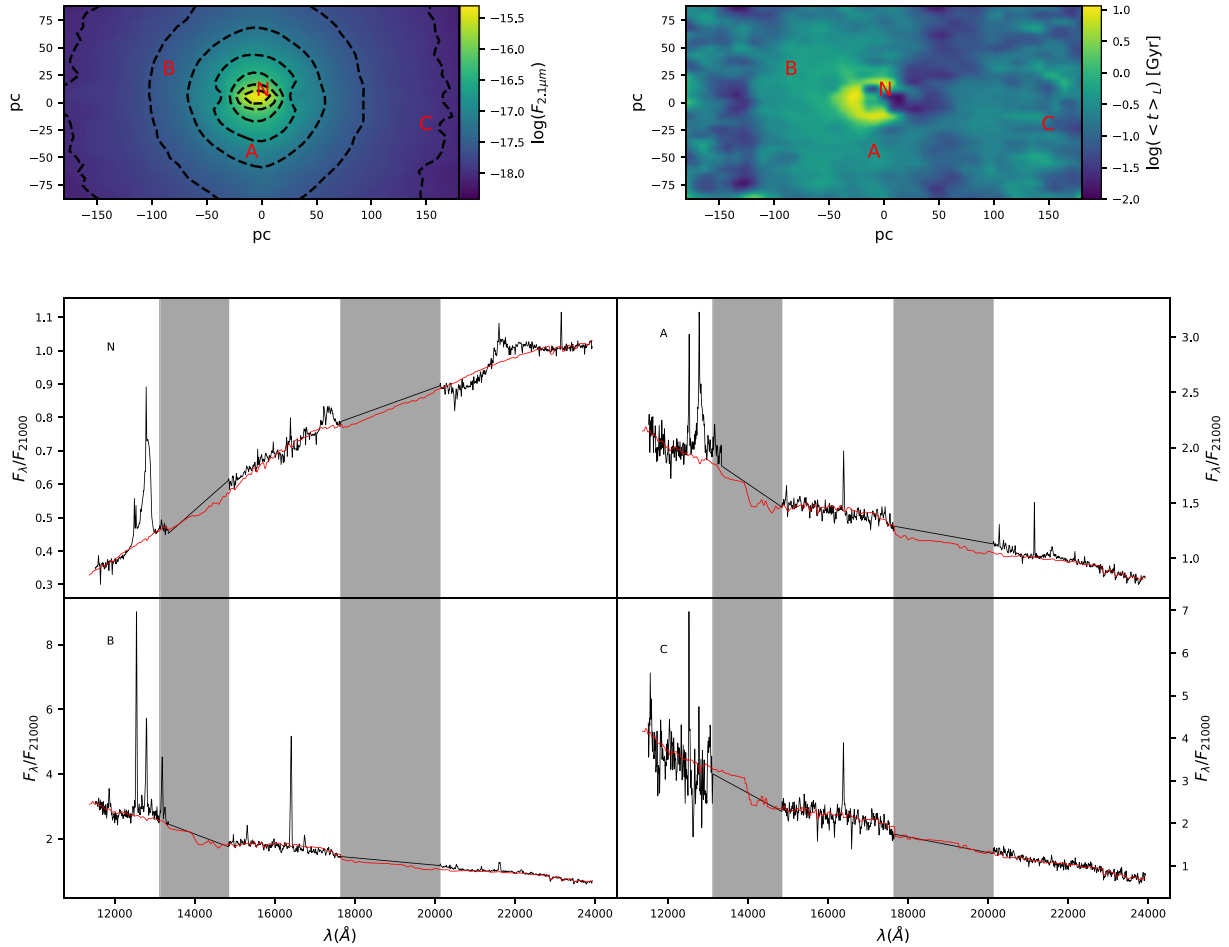


Figure 2. In top panels, we show continuum (left) and light-weighted mean age (right) maps for NCG 4151. In the bottom panels, we show examples of four single spaxels fits: the nuclear region and other three distinct locations identified in the top panels. This is the only galaxy with *J*, *H*, and *K* bands available.

FoV reaching 20 per cent, and no FC emission is detected. The mean age map shows that the central region of this galaxy is dominated by populations with ages smaller than 1 Gyr, decreasing outwards.

NGC 1068. This source has a very complex SFH, with the unresolved nuclear region being dominated by the HD component. Outside this region, large fractions of the HD are also observed. Its stellar content is dominated by young and intermediate-age populations. A detailed analysis of the stellar populations of this galaxy is made in Martins et al. (2010) and Storch-Bergmann et al. (2012).

NGC 2110. In terms of stellar content the central region of this galaxy is dominated by intermediate-age and old stellar populations, with a smaller fraction in the *xy* component. It also shows a large fraction of HD emission in the unresolved nucleus. A detailed study of the stellar populations of this galaxy is presented in Diniz et al. (2019).

NGC 3227. Very small fractions of the two younger SPC are detected. An off-centred ($x = 60$ pc, $y = -20$ pc) ring-like structure of intermediate young (*xy*) stars can be seen and a significant fraction of *xio* SPC is detected over the entire FoV. This structure has a very good agreement with the off-centre, ring-like structure found in CO(2–1) Atacama Large Millimeter/submillimeter Array (ALMA) observations by Alonso-Herrero et al. (2019, 2020), as well as with a low velocity dispersion stellar ring (Barbosa et al. 2009) and in Pa α

emission (Bianchin et al. 2022), indicating that this gas reservoir is forming stars. We note that a vertical stripe is seen to the west side of the FoV and that this feature should be treated with caution. The old SPC is also detected over the entire FoV contributing 25 per cent, except for the unresolved nucleus ($r \leq 15$ pc), which is dominated by HD emission (75 per cent) together with 10 per cent of FC emission. The mean age map shows that NGC 3227 is dominated by stellar populations with ages lower than 2 Gyr.

NGC 3516. A partial ring of the *xy* SPC is observed from west to east towards the south locations, starting at 30 pc out to the end of our FoV (150 pc). No *xyo* population was required. A clear ring ($100 < r < 150$ pc) of *xy* stars is detected surrounding a ring of the *xio* component (with a smaller contribution of *xo*). This ring surrounds a nuclear unresolved ($r < 30$ pc) HD and FC emission. The mean age map shows that this source is dominated by a population younger than 1.5 Gyr.

NGC 4151. This galaxy displays a strong contribution of young SPCs. The *xy* population is clearly detected on the west side of the FoV, summing up 50 per cent contribution, as well as on the east side, starting at 100 pc from the nucleus up to the edge of the FoV. A ring-like structure ($\sim 30 < r < 150$ pc) composed predominantly of the *xy* SPC, which is responsible in some locations for up to 75 per cent of the emitted light, can be seen in the maps. Small fractions of *xyo* (≤ 30 per cent) stars can also be found in this ring-like structure. This

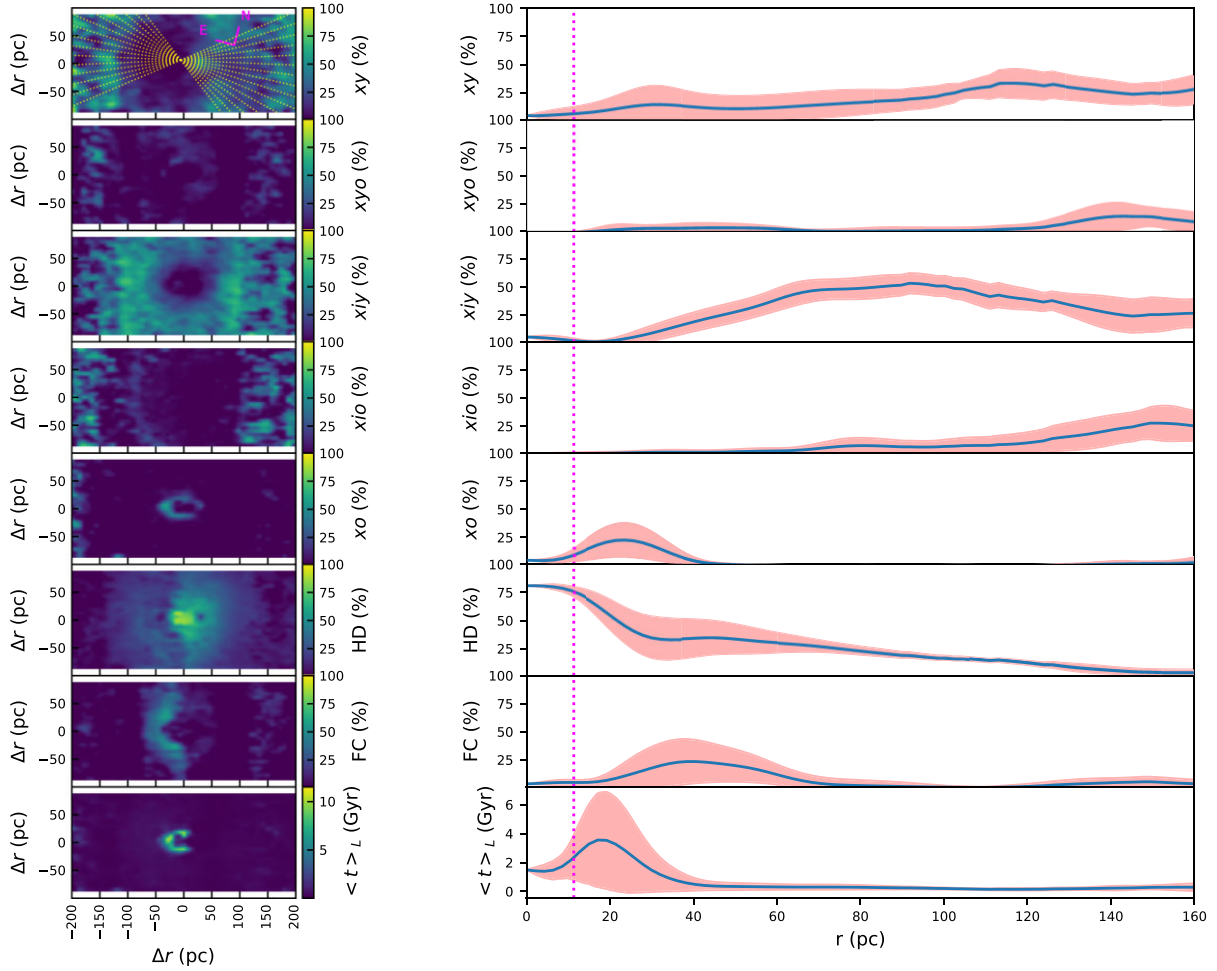


Figure 3. Maps and radial profiles for NGC 4151. Left-hand side, from top to bottom: xy per cent contribution of SSPs with ages $t \leq 50$ Myr; xyo per cent contribution of SSPs with ages in the range $100 \leq t \leq 200$ Myr; xiy contribution of SSPs with ages in the range $500 \leq t \leq 700$ Myr; xio contribution SSPs with ages in the range $1 \leq t \leq 2$ Gyr; xo contribution $5 \leq t \leq 13$ Gyr; HD contribution of all Plank functions components; FC is the featureless continuum per cent contribution; $\langle t \rangle_L$ is the light-weighted mean age. In the right-hand side we show the radial profiles (yellow dotted lines on the first panel) showing the azimuthal mean of the corresponding properties, together with their standard deviation (shaded region). The dotted vertical line is the PSF of the FWHM taken from Riffel et al. (2017, 2021b). We have identified spaxels with a percentage mean deviation (Adev_S) larger than 10 (red contour) and 20 (white contour) per cent. See text for more details.

component surrounds a nuclear ($r < 40$ pc) contribution from an old population. A very strong contribution of HD emission is observed in the unresolved nucleus ($r \lesssim 10$ pc) of this source and extends towards the full FoV. The FC component is also seen up to $r \sim 60$ pc. With the nucleus being dominated by HD emission, the mean age map shows a ‘hole’, with a peak of ~ 5 Gyr SPC at 20 pc from the centre, beyond which it has a strong negative gradient out to 40 pc and then is nearly constant ($t \sim 500$ Myr) in the rest of the FoV.

NGC 4235. This galaxy shows a very complex SFH over the full FoV. A (partial) ring of xy is clearly present, with values reaching 50 per cent to northern ($r > 130$ pc) and western ($r \gtrsim 100$ pc) locations, where a vertical stripe can also be seen, and which may be attributed to a residual fingerprint. Small fractions (≤ 20 per cent) of the xyo SPC are detected in NW and south-east (SE) directions ($r \gtrsim 130$ pc), while a partial ring of intermediate population (xiy and xio) is detected towards east–south–west directions surrounding the centre ($50 < r < 150$ pc). The xo component shows up on the full FoV with values reaching 50 per cent. A clear dominance (75 per cent) of HD emission is seen in the unresolved nucleus ($r < 25$ pc) with a contribution of FC emission of less than 20 per cent. The HD component shows a steep

gradient decreasing out to the edge of the FoV ($r \sim 200$ pc), while the FC seems to reach its maximum (20 per cent) for $r \sim 40$ pc towards SE directions. The mean age map shows the light is dominated by a 500 Myr population with a flat gradient, rising up again outwards of ~ 200 pc.

NGC 5506. The two youngest SPC show a negligible contribution to the integrated spectrum emission of this galaxy. A ring-like structure ($90 < r < 120$ pc) is observed for the xiy component, while for the two oldest components an arc structure is observed towards the west direction ($r > 90$ pc) with a maximum value of 25 per cent for the xo . The dominant feature we have detected in this source is the HD emission, completely dominating the nuclear emission. Meanwhile, no contribution of the FC component was found in the nuclear region, although it reaches up to ~ 50 per cent in the outer regions of the FoV ($r > 90$ pc). We interpret this as due to HD emission instead of scattered light from the AGN. The mean age map also shows the ring signature pointing to very young ages in the centre. This, however, seems to be a fitting artefact, since the nuclear emission reaches ~ 100 per cent for the HD emission.

NGC 5548. The FoV of this galaxy is dominated by the xo population, with a ring ($r > 200$ pc) of xyo populations. HD and FC are detected along the full FoV. A detailed analysis is made by Schönell et al. (2017).

NGC 5899. The two youngest components show a small contribution over the FoV, with an enhancement to the west/NW side (~ 75 per cent for $r > 100$ pc in this side). The intermediate-age components are clearly the dominant ones with xiy being enhanced on the east side of the FoV (where it reaches a ~ 75 per cent contribution). The xio SPC is well distributed over the FoV with a mean value of ~ 40 per cent in the inner 100 pc radius. For the old SPC we can see a flat distribution over the entire FoV, with a contribution of ~ 20 per cent. Very small fractions of HD and FC are required in the central region and the mean age shows a small gradient with values dropping from ~ 1.3 to ~ 0.7 Gyr in the outer regions.

NGC 5929. A very small fraction of xy SPC is observed SE of the nucleus ($r > 110$ pc) of NGC 5929, while no signs of the xyo component are seen. The dominant emission of the central region is due to the xiy SPC reaching 75 per cent in most locations of the FoV, and presenting a value of 25 per cent in the unresolved nucleus ($r < 25$ pc), which is dominated by the xio population (up to 50 per cent). No HD and FC emission are detected. The mean age shows a decreasing gradient with ages between 1.5 Gyr in the nucleus and 0.6 Gyr in the outermost locations ($r \sim 100$ pc).

Mrk 607. The SFH of the central region of this galaxy is very complex and all the SPCs are necessary to explain the continuum emission of this galaxy. The two youngest SPCs (xy and xyo) when taken together present a partial ring, from south towards west up to north ($130 < r < 150$ pc). The xiy SPC shows another ring-like structure ($100 < r < 150$ pc), reaching up to 50 per cent of the emission. The xio SPC is spread over the FoV, and summed with xo contributes up to 40 per cent of the stellar emission in the nuclear region ($r < 50$ pc). The clear dominant nuclear emission in this galaxy is due to the HD emission, reaching more than 50 per cent in the centre, and falling to zero in the outer locations. A tiny fraction (< 5 per cent) of an FC is also detected in the unresolved nucleus. The mean age shows a decreasing gradient, with a peak of ~ 2.5 Gyr in the centre falling to values $\lesssim 1$ Gyr in the outer locations.

Mrk 766. This source also shows a very complex SFH, with a ring of very young (xy) stars dominating the emission in the outer regions of the FoV ($r \gtrsim 200$ pc). In this same ring there is a coexistence of all other SPCs, in smaller fractions. The centre is dominated by HD (~ 60 per cent) and FC (~ 30 per cent) emission. The mean age map indicates that slightly older stars are located in a SE direction.

Mrk 1066. The FoV of this galaxy is dominated by the xiy population. HD and FC emission are clearly observed in the unresolved nucleus, decreasing outwards over the full FoV. A detailed analysis is made by Riffel et al. (2010).

Mrk 1157. The FoV of this galaxy is dominated by the intermediate-age populations (xiy and xio) with a smaller contribution of xo . Small fractions of HD and FC emission are observed in the unresolved nucleus. A detailed study of the stellar populations for this galaxy is made in Riffel et al. (2011c).

To summarize the individual results, we have plotted in Fig. 4 the individual profiles of the binned population vectors. These figures show the results for all the 18 galaxies, including the six objects previously studied by our group. It is clear from this figure that the inner region has centrally peaked HD emission in the unresolved region (dotted line). On the other hand, for the FC contribution we found that for nearly half of our sample this component reaches the highest values outside the unresolved nucleus (see Section 4.3).

In terms of stellar populations, the galaxies show a considerable fraction of young ($xy + xyo$) stellar populations; however, the central region is dominated by an intermediate-age population ($xiy + xio$), as well as a significant fraction of old stars. In general, the galaxies display a very complex SFH in the central region.

4.2 Sample results

In order to compare the stellar population results for our sample with the properties listed in Table 1, we have followed Riffel et al. (2021b) and have computed the mean values of the derived stellar population properties inside a 125 pc radius. These values are listed in Table 2. It is worth mentioning that since we are taking the mean value over the 125 pc in centre of the galaxies, the possible fingerprints left on the borders of the FoV do not play an important role on the obtained values.

When merging Tables 1 and 2 data together we are left with a large set of properties. To compare all the properties we have computed the Pearson standard correlation coefficient matrix using the SEABORN statistical data visualization PYTHON package (Waskom 2021). The diagonal correlation matrix is shown in Fig. 5 where the triangle traced by dashed lines shows the correlation coefficients of properties obtained by derivations that may depend on each other ($\log(L_X)_{\text{obs}}$, $\log(L_X)_{\text{int}}$, $\log(L_{\text{Bol}})_{\text{obs}}$, $\log(L_{\text{Bol}})_{\text{int}}$, σ_* , $\log(M_{\text{SMBH}})$, $\log(L_{\text{Edd}})$, λ_{obs} , λ_{int} , and redshift) and therefore will not be discussed here, but are left in the figure for completeness.

4.3 Caveats on hot dust versus featureless continuum: possible degeneracies

Our analysis points towards the detection of HD and/or FC outside the unresolved nucleus in nearly half of the sources (NGC 4151, Mrk 79, NGC 3227, NGC 3516, NGC 4235, NGC 5506, Mrk 766, NGC 1068, NGC 2110, NGC 5548, and Mrk 1066).

The case of the FC component is a known and common problem in the study of the stellar content of Seyfert galaxies. It is related to the fact that the continuum of a reddened young starburst ($t \lesssim 5$ Myr) is indistinguishable from an AGN-type continuum, which is why we have not added such young ($t < 10$ Myr) components in the base of elements (for more details see Riffel et al. 2009, and references therein). This could be used to explain the fact of the FC component showing up outside the unresolved region, in the case of regions dominated by the very young populations (J or $J + H$ bands dominated by young stellar populations). In this case, this fraction would not be a true AGN component, but due to a very young reddened stellar population.

As can be seen from Fig. 1 a degeneracy between FC and BB components can occur when the HD (or FC) dominates the K -band emission and the stellar population dominates the J band (or $J + H$). In that case, the main distinguishing characteristic will be the slope of the continuum in the K band. In this case, the FC component is hardly distinguishable from dust with $T \gtrsim 1200$ K. In contrast, in situations where either stellar light dominates all three bands (i.e. away from the nucleus), or the HD + FC dominate all bands (right on the nucleus), there will be no issue. The degeneracy will only show up in the transition regions. In order to test this, we performed a fit in which we only included the FC component in the central ($r = 2$ pixels) unresolved region. For the cases where there had been some fraction of FC in the outer region, this was now redistributed among the BB components, with very little going into the SSP components.

Complementing these tests is the fact that the $\log(L_{\text{Bol,obs}})$ and FC correlation is only strong for larger fractions of FC. We interpret

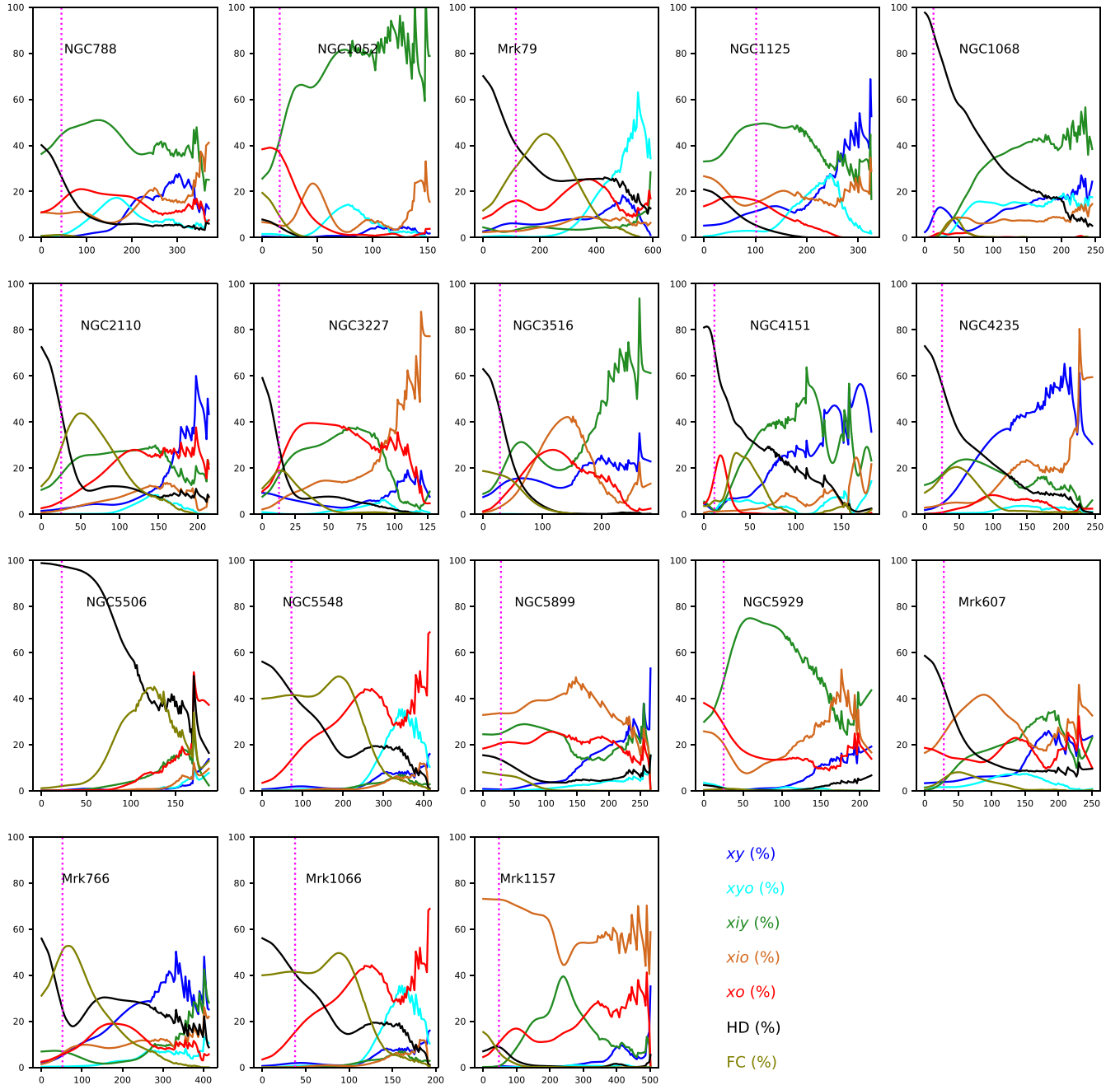


Figure 4. Individual profiles for each population vector. The dotted vertical line is the PSF of the FWHM taken from Riffel et al. (2017, 2021b). It can be seen that the SFH of these sources is complex, the HD component dominates the emission of the unresolved nucleus for almost all the sources, while the FC reaches its maximum value for some galaxies outside the nucleus. Very high fractions of young to intermediate-age stars are observed in regions with ($r \gtrsim 100$ pc). See text for more details.

this as implying that when there is a significant FC fraction (≥ 15 per cent), it can be associated with the accretion disc emission. This result is in agreement with the fact that broad components in polarized light are associated with larger fractions of the FC component (Cid Fernandes & Terlevich 1995; Cid Fernandes et al. 2004; Riffel et al. 2009).

These results, taken together with the fact that HD emission outside the unresolved region has been previously reported in AGNs (e.g. Davies et al. 2005; Dottori et al. 2005; Grataour et al. 2006; Martins et al. 2010; Storchi-Bergmann et al. 2012; Gaspar et al. 2019), makes us to interpret the FC detected in the transition regions

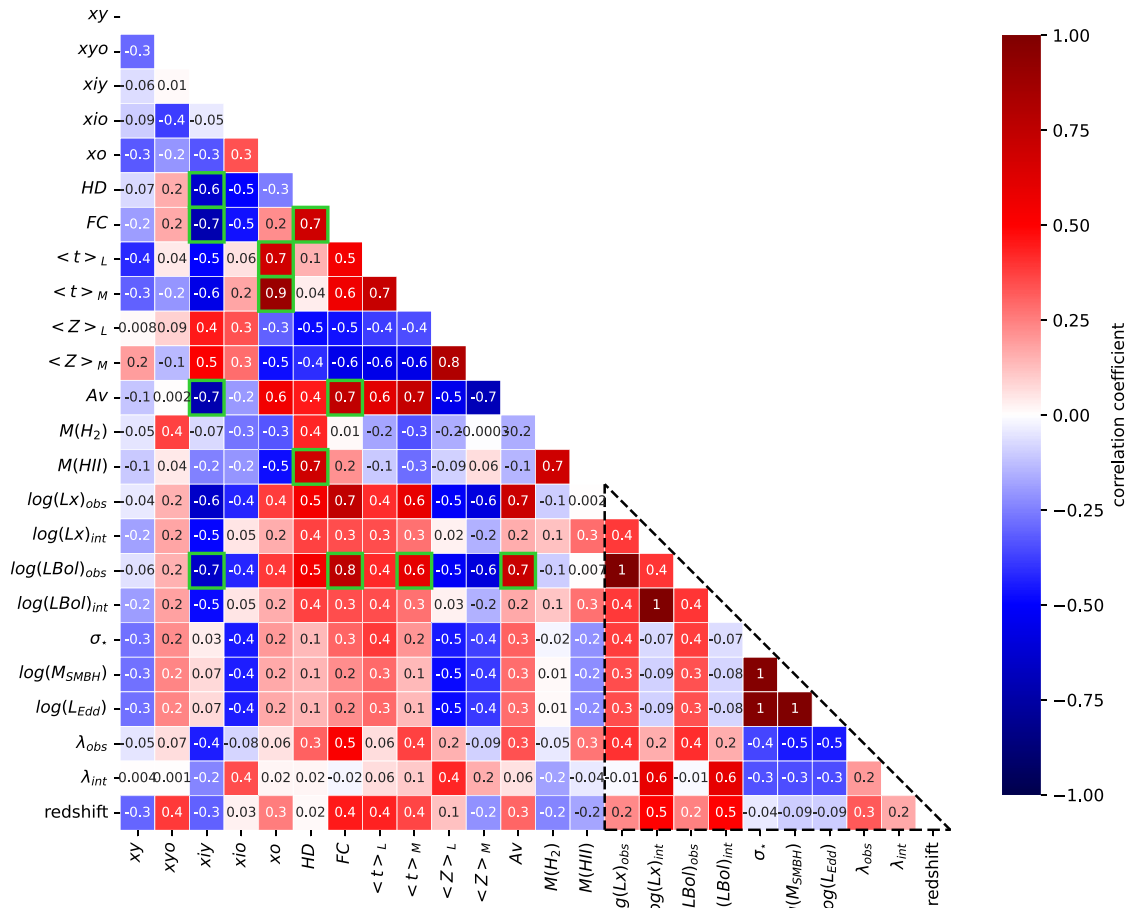
(outside the unresolved region) as due to HD emission (which, in that case, would be heated by young stellar populations) or to a reddened very young stellar population, and not to a true AGN FC component.

5 DISCUSSION

When inspecting the correlation matrix (Fig. 5) we see that several quantities are well correlated ($|R| > 0.5$). After removing the possible correlations with $L_{X_{\text{obs}}}$, since they should be the same as those with $L_{\text{Bol}_{\text{obs}}}$ (that was derived using $L_{X_{\text{obs}}}$), we have made scatter plots

Table 2. Mean values of the derived stellar population properties within the inner 125 pc.

Source	xy	x_{yo}	x_{iy}	x_{io}	x_o	HD	FC	$\langle I \rangle_L$	$\langle I \rangle_M$	$\langle Z \rangle_L$	$\langle Z \rangle_M$	A_V
NGC 788	2.23 ± 4.72	8.9 ± 13.54	48.77 ± 19.72	15.52 ± 19.77	15.66 ± 11.6	8.9 ± 10.53	0.0 ± 0.02	0.94 ± 0.43	3.21 ± 2.14	0.03 ± 0.01	0.02 ± 0.01	0.41 ± 0.39
NGC 1052	3.28 ± 7.77	11.36 ± 14.84	73.18 ± 21.53	7.66 ± 17.77	3.87 ± 9.8	0.21 ± 1.35	0.44 ± 3.43	0.6 ± 0.46	1.27 ± 1.75	0.03 ± 0.01	0.03 ± 0.01	0.11 ± 0.45
Mrk 79	5.43 ± 7.45	19.08 ± 29.08	8.38 ± 10.92	2.91 ± 3.49	11.55 ± 14.26	28.45 ± 23.73	24.21 ± 27.1	1.01 ± 1.14	3.61 ± 3.21	0.02 ± 0.01	0.01 ± 0.01	2.0 ± 1.36
NGC 1125	15.9 ± 17.19	7.57 ± 11.05	48.36 ± 29.79	15.89 ± 18.44	7.87 ± 13.34	4.42 ± 6.03	0.0 ± 0.0	0.57 ± 0.55	1.9 ± 2.83	0.03 ± 0.01	0.03 ± 0.01	0.08 ± 0.23
NGC 1068	10.66 ± 7.04	13.05 ± 8.37	29.47 ± 16.41	10.67 ± 12.11	0.77 ± 1.94	34.17 ± 19.21	1.22 ± 3.14	0.29 ± 0.16	0.64 ± 1.23	0.02 ± 0.01	0.02 ± 0.01	0.25 ± 0.74
NGC 2110	12.35 ± 14.77	1.64 ± 5.08	24.04 ± 10.58	7.94 ± 9.47	19.2 ± 13.33	16.11 ± 15.28	18.72 ± 17.27	0.97 ± 0.75	5.41 ± 2.51	0.02 ± 0.01	0.02 ± 0.01	1.5 ± 0.79
NGC 3227	5.4 ± 9.18	2.49 ± 6.48	28.21 ± 21.07	27.29 ± 27.52	28.87 ± 16.73	5.45 ± 8.54	2.28 ± 6.19	1.56 ± 0.93	5.13 ± 2.51	0.02 ± 0.01	0.02 ± 0.01	1.95 ± 0.69
NGC 3516	15.85 ± 14.19	0.02 ± 0.13	30.79 ± 25.01	21.64 ± 18.96	22.59 ± 15.73	5.68 ± 15.79	3.44 ± 11.53	0.92 ± 0.71	4.97 ± 2.81	0.01 ± 0.01	0.01 ± 0.01	1.29 ± 0.94
NGC 4151	37.39 ± 28.46	2.76 ± 5.66	25.36 ± 22.26	9.12 ± 13.8	5.12 ± 12.03	16.54 ± 17.17	3.71 ± 8.93	0.39 ± 1.25	1.62 ± 3.08	0.02 ± 0.01	0.02 ± 0.01	0.16 ± 0.73
NGC 4235	29.84 ± 23.03	2.38 ± 5.97	21.93 ± 17.79	10.95 ± 13.6	4.77 ± 7.93	22.14 ± 19.48	7.98 ± 13.42	0.33 ± 0.4	1.93 ± 2.19	0.02 ± 0.01	0.02 ± 0.01	2.1 ± 1.06
NGC 5506	1.06 ± 2.67	0.7 ± 4.16	8.94 ± 10.36	2.93 ± 6.21	6.78 ± 11.57	56.83 ± 36.61	22.76 ± 26.14	1.37 ± 1.83	3.23 ± 3.46	0.01 ± 0.01	0.01 ± 0.01	1.83 ± 2.05
NGC 5548	5.9 ± 8.85	9.54 ± 16.12	2.39 ± 8.5	2.82 ± 8.68	26.7 ± 21.34	25.13 ± 24.12	27.51 ± 28.59	3.95 ± 3.75	6.62 ± 3.12	0.01 ± 0.01	0.0 ± 0.0	2.96 ± 1.78
NGC 5899	14.84 ± 23.44	4.89 ± 10.73	25.27 ± 26.85	28.96 ± 25.96	19.1 ± 14.53	5.41 ± 7.83	1.53 ± 4.12	1.11 ± 0.86	4.5 ± 2.8	0.02 ± 0.01	0.01 ± 0.01	1.7 ± 0.85
NGC 5929	2.71 ± 6.09	3.25 ± 10.14	61.07 ± 25.42	17.4 ± 23.7	14.42 ± 13.33	0.82 ± 1.81	0.31 ± 1.64	0.94 ± 0.48	3.32 ± 2.2	0.02 ± 0.01	0.01 ± 0.01	0.61 ± 0.71
Mrk 607	13.51 ± 17.54	5.56 ± 10.75	20.99 ± 18.78	27.31 ± 21.68	14.39 ± 15.39	15.3 ± 11.83	2.94 ± 5.61	1.23 ± 1.07	3.78 ± 3.15	0.03 ± 0.01	0.02 ± 0.01	1.45 ± 0.83
Mrk 766	11.51 ± 10.5	2.94 ± 7.15	4.44 ± 8.54	18.05 ± 18.5	15.3 ± 15.16	25.87 ± 20.03	21.88 ± 21.12	1.23 ± 1.35	5.91 ± 3.39	0.03 ± 0.01	0.02 ± 0.01	2.02 ± 1.08
Mrk 1066	18.88 ± 30.18	1.1 ± 2.23	61.55 ± 31.87	6.75 ± 13.09	4.85 ± 7.17	5.96 ± 9.7	0.91 ± 2.11	0.47 ± 0.3	1.45 ± 1.29	0.03 ± 0.01	0.03 ± 0.01	0.35 ± 0.48
Mrk 1157	5.65 ± 10.28	0.42 ± 1.97	19.71 ± 26.67	55.3 ± 31.6	15.48 ± 14.83	2.03 ± 3.02	1.41 ± 3.4	1.63 ± 0.92	3.52 ± 1.92	0.03 ± 0.0	0.03 ± 0.01	0.22 ± 0.3


Figure 5. Diagonal Pearson standard correlation coefficient matrix comparing the sample properties and derived stellar population properties. The triangle represented with dashed lines shows the coefficients of properties obtained from literature or which derivation is dependent with each other. The meaningful correlations are plotted in Fig. 6 and are highlighted with green boxes. For details see text.

for all potential correlations ($|r| > 0.5$). These are shown in Fig. 6 together with a linear fit to the data points (dotted blue line) obtained using bootstrap realizations (Davison & Hinkley 1997) with the Huber regressor model that is robust to outliers (Owen 2007). The Pearson's correlation coefficient (R), slope (a), and intercept (b) are also quoted. The uncertainties on the correlation coefficients are the standard deviation of the mean after 1000 bootstrap realizations. We have only considered as statistically significant correlations where

the difference between the modulus of the mean R value minus the standard deviation was larger than 0.45 ($|R| - \delta R > 0.45$). From this we got the following meaningful correlations: $x_{iy} \times \text{HD}$; $x_{iy} \times \text{FC}$; $x_{iy} \times A_V$; $x_{iy} \times \log(L_{\text{Bol,obs}})$; $x_o \times \langle I \rangle_L$; $x_o \times \langle I \rangle_M$; $\text{HD} \times M(\text{HII})$; $\text{HD} \times \text{FC}$; $\text{FC} \times A_V$; $\text{FC} \times \log(L_{\text{Bol,obs}})$; $\langle I \rangle_M \times \log(L_{\text{Bol,obs}})$, and $A_V \times \log(L_{\text{Bol,obs}})$.

A clear anticorrelation of the intermediate young (x_{iy} ; 500 Myr $\leq t \leq 700$ Myr) SPC with the two featureless AGN components (HD

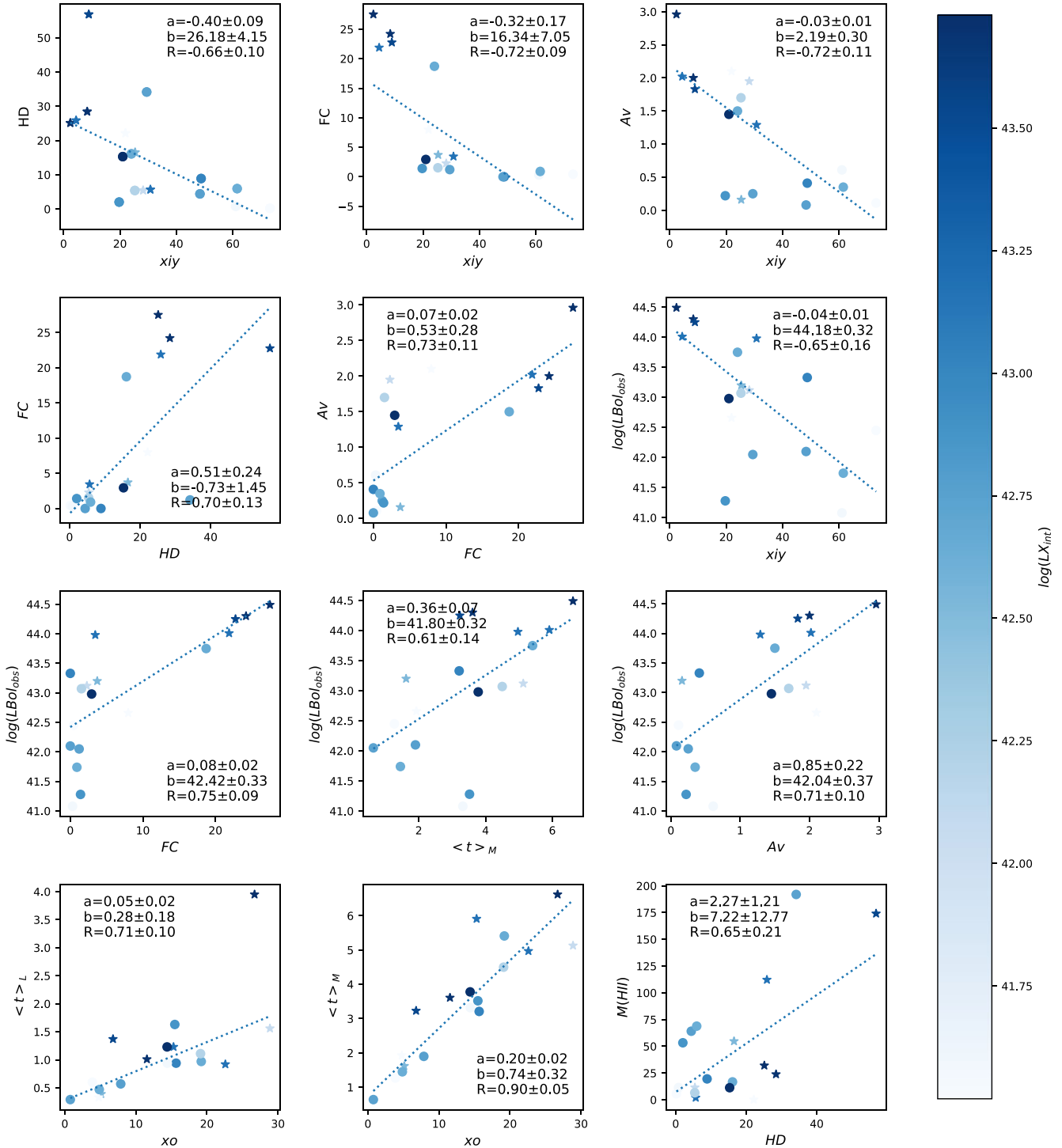


Figure 6. Correlations of different properties (stars represent Sy 1 and circles Sy 2). The uncertainties on the linear fit (dotted blue line, $y = ax + b$) to the data points (circles) were obtained using 1000 bootstrap realizations with Huber regressor model. The Pearson's correlation coefficient (R), slope (a), and intercept (b) are labelled. The error bars for a and b are the standard deviation of the mean after the bootstrap realizations. We have only considered as statistically significant correlations were the difference between the absolute mean r value minus the standard deviation was larger than 0.45 ($|R| - \delta R > 0.40$). The blue dotted line is obtained with the mean a and b values. The logarithmic of the X-ray intrinsic luminosity is represented by different colours. For details see text.

and FC) and reddening is observed. This is further confirmed by the correlation of FC and HD and A_V and FC, since these quantities are individually related with x_{iy} .

In addition, x_{iy} is also anticorrelated with the logarithm of the observed bolometric luminosity and there is a trend in the sense that

higher intrinsic X-ray luminosity is observed for higher fractions of HD, FC, and A_V (see Fig. 6).

The correlation between the X-ray luminosity (seen via the correlations with L_{Bol}) and HD, FC, and A_V can be tentatively attributed to the fact that all these properties are linked to the mass accretion

rate on to the AGN, as follows. More A_V means more gas, thus more fuel to the AGN, and more fuel results in increased accretion rate. This in turn leads to higher luminosity of the accretion disc, thus increased contribution of the FC continuum. This continuum is the source of the heating of the circumnuclear dust, and thus the HD contribution also increases. A closer look at these plots (third row of panels in Fig. 6) shows that the correlation is dominated by the most luminous sources ($\log(L_{\text{Bol}}) \geq 43.5$) and can be understood as due to the fact that, for the low-luminosity end, secondary parameters may play an important role (see Yang et al. 2015, for example).

The anticorrelation of the above properties with x_{iy} may be a secondary effect, resulting from the fact that all of them are correlated, meaning that, when all their contributions increase, the result is a decreased contribution of the stellar population.

The mean ages (light and mass weighted) are well correlated with the x_0 component and a tighter correlation is observed between x_0 and $\langle t \rangle_M$, due to the non-linear behaviour of the M/L fractions of stellar populations (see Riffel et al. 2009, for additional discussion). However, it is important to note that the fractions of x_0 are less than 30 per cent and that the mean age is actually dominated by the younger components (see equation 3).

HD is correlated with the mass of H II and with the FC fraction, suggesting that the HD present in the inner region of these galaxies is heated by the AGN FC. This is in agreement with the previous interpretation: more gas means increased accretion rate, increasing the FC, which increases the heating of the dust, resulting in a larger HD fraction.

As expected $\log(L_{\text{Bol,obs}})$ is well correlated with the FC fraction, since the bolometric luminosity is primarily driven by the AGN accretion disc emission. This correlation is very strong for $\text{FC} \geq 15$ per cent, while for small values of FC a scatter is observed (see Section 4.3).

A correlation of $\log(L_{\text{Bol,obs}})$ and $\langle t \rangle_M$ is also observed. This correlation remains when, instead of the mass-weighted mean ages, we use the light-weighted ones. However, it is weaker, but in the case of light-weighted mean ages the values for almost all sources are $\langle t \rangle_L \lesssim 1.5$ Gyr. We interpret this correlation as due to a delay between the formation of new stars and the triggering/feeding of the AGN. The cold gas that reaches the SMBH most probably is originated from the mass loss from intermediate-age stars, as proposed by Davies et al. (2007) who found that star formation inhibits accretion, and that gas accretion into the SMBH is only efficient after these early turbulent phases of stellar feedback. The gas released by this intermediate-age population has a low velocity (a few hundred km s^{-1}) and is accreted together with the gas already available in the central region (e.g. Cuadra et al. 2006; Hopkins 2012). This extra amount of gas will trigger the AGN (or make it brighter). The intermediate-age population is dominated by C- and O-rich stars (e.g. Dottori et al. 2005; Maraston 2005; Riffel et al. 2007, 2015; Salaris et al. 2014), and these short-lived stars ($t \simeq 0.2\text{--}2$ Gyr; $M \simeq 2\text{--}6 M_\odot$) do release enriched material to the nuclear environment (fuelling the AGN). This material would remain, held back by the central potential, and may explain the HD that is observed outside the unresolved nucleus.

We also compared our findings with the optical stellar population results of Bartscher et al. (2021). They analysed the inner 150 pc of nine AGN hosts from a complete volume-limited sample of targets with $L_{14\text{--}195 \text{ keV}} > 10^{42.5}$ from the Local Luminous AGN with Matched Analogues (LLAMA) sample. Out of their nine AGNs, they detected young stellar populations in seven. On average, the light

contribution⁴ from these young stellar populations was 4.5 per cent, compared to 11.8 per cent in our sample. Another difference between our results and theirs is the fact that in all their AGNs except one, the light is dominated by old stellar populations, whereas this is the case for only two of our galaxies (NGC 3227 and NGC 5548). A similar analysis was done by Dahmer-Hahn et al. (2022), who analysed the stellar populations using optical integral field unit (IFU) data of 14 AGN (being the optical counterpart of the present sample). Similarly to the results of Bartscher et al. (2021), nine of their objects have evidence of young stellar populations in the inner 150 pc, with an average light contribution of 7 per cent. Also, their sample is also dominated by old stellar populations, with more than 70 per cent of the light coming from stellar populations older than 2 Gyr stellar populations.

Compared to these optical works, we detected young and intermediate-age stellar populations in a higher fraction of galaxies, and with a higher average contribution. This is a direct consequence of the lower reddening effects in the NIR, meaning that we can access stellar populations that are inaccessible in the optical due to dust obscuration, together with the fact that the NIR is more sensitive to the colder bright stellar phases (Maraston 2005; Riffel et al. 2011a,b, 2015; Salaris et al. 2014).

As discussed above, in Fig. 6, we have obtained a mean value of the stellar population properties for the inner 125 pc of each galaxy. In order to better understand the variation of these properties as a function of distance to the nucleus, we have computed mean and median profiles inside this region (which is the full FoV in the case of NGC 3227) for the full sample. The resulting profiles are presented in Fig. 7, as well as the corresponding standard deviations.

What emerges from this exercise is that the inner few parsecs ($r \lesssim 40$ pc) of the galaxies have their emission dominated by HD emission and in terms of stellar content they are dominated by intermediate-age stellar populations (x_{iy} and x_{yo}). This is reflected by the $\langle t \rangle_L$ profile, which is nearly constant (~ 1 Gyr) over the inner 125 pc, reaching a maximum value of ~ 2 Gyr.

In order to better understand the radial behaviour of the SFH over our sample we have produced mean values for the SPCs of our sample in four radial bins.⁵ The result of this procedure is shown in Fig. 8, where we show the mean values for the HD, FC, x_y , x_{yo} , x_{iy} , x_{io} , and x_0 for the different radial bins (in red for $r < 50$ pc, in blue for $50 < r < 100$ pc, in green for $100 < r < 150$ pc, and in magenta for $150 < r < 200$ pc). What emerges from this plot is that the HD and FC components decrease outwards; x_y and x_{yo} increase from small to larger scales; while x_{iy} , x_{io} , and x_0 are nearly constant over the FoV (showing a small trend to increase outwards).

We interpret this result as the fact that the AGN is impacting on the recent star formation, in the sense that it can be associated with the decrease of young star formation towards the nuclear region. Another interesting point is that all the components older than x_{io} ($t \gtrsim 500$ Myr) are nearly constant over the FoV. We speculate that this maybe because of any episodic nature of the star formation rate is removed on those longer time-scales. In particular, especially for x_{io} and x_0 , we are looking at bulge stars along the line of sight that one would not expect to be affected by what is going on in the disc plane at small scales.

⁴It is worth mentioning that the comparison of optical and NIR young stellar populations is not direct (Riffel et al. 2011b).

⁵The mean value over the profiles shown in Fig. 7 inside the four regions.

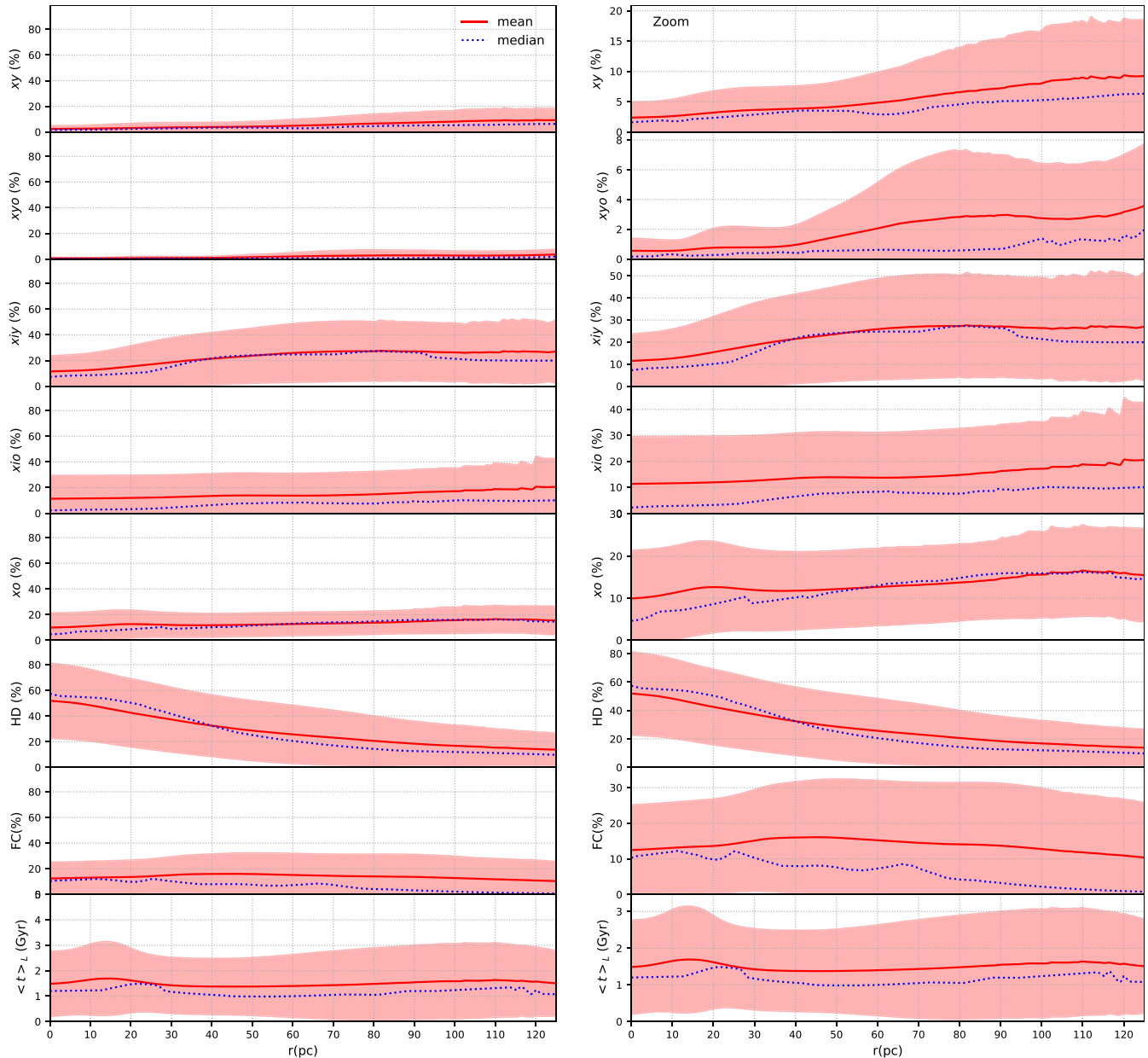


Figure 7. Mean and median AGN profiles of different properties (left to the same scale and right a zoom in). These profiles were obtained as the mean/median values of the individual profiles for each AGN (see Fig. 3 and the supplementary material, for example). The red shaded regions are the standard deviation. It is clear from that figure that the inner pc of the galaxies is dominated by an intermediate-age stellar population.

When inspecting the $FC \times HD$ panel of Fig. 6 we observe that on one hand the correlation becomes weaker for higher fractions of FC (the same regime where $\log(L_{\text{Bol,obs}})$ and FC show a tight correlation). On the other hand, for the case of low FC ($\lesssim 5$ per cent), HD tends to be low too. As can be seen in Fig. 6 the majority of these points cover a wide range of L_X and A_V . We suggest that in these cases either the luminosity is low or they are much obscured, so that no FC leaks out and even the HD, in these central regions ($r < 125$ pc), is hidden.

This is further supported by the fact that there is only a small correlation between HD and $\log(L_{\text{Bol,int}})$ (Fig. 5). We interpret this as due to the inclusion of both type one and type two sources in our analysis, and the fact that HD emission is more common in Sy 1 than in Sy 2s (Riffel et al. 2009). In addition Burtscher et al. (2015) showed that there is a good correlation between HD and AGN luminosity (fig.

9 of that paper) for Sy 1, but the Sy 2 is offset by about an order of magnitude with a larger scatter. They associate this with a general reduction in the derived apparent HD temperature from type 1 to type 2 sources, with both effects being due to extinction.

6 CONCLUSIONS

We present a spatially resolved stellar population study of the inner few tens of pc in a volume-limited complete sample of nearby AGNs. This study was performed with adaptive-optics-assisted observations in the NIR. Our main results are summarized as follows.

- (i) In general, the galaxies display a very complex (e.g. many components are required to fit the underlying continuum) SFH in the central region.

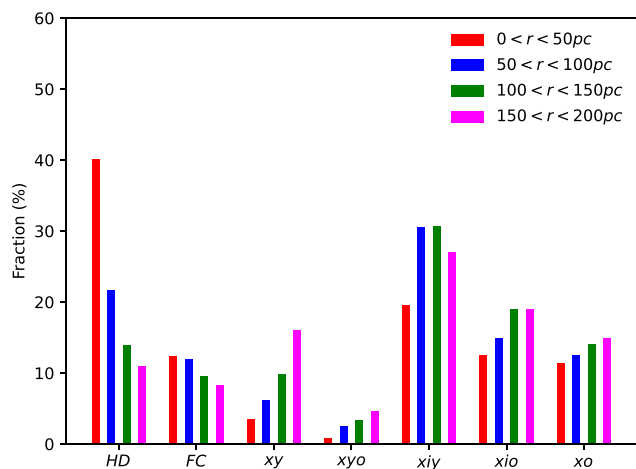


Figure 8. Histogram of average population vectors (labelled) for different radial bins (see labels). HD and FC components decrease outwards, while xy and xyo increase outwards. The intermediate population dominates the emission over the full FoV with a trend of increasing outwards. xo is nearly constant over the full FoV.

(ii) In terms of stellar populations, the light in the FoV of the galaxies is due to a considerable fraction of young ($xy + xyo$) stellar populations. The central region is dominated by an intermediate-age population ($xiy + xio$), with a significant fraction of old bulge stars.

(iii) The inner region of the galaxies has centrally peaked HD emission inside the unresolved region. On the other hand, for the FC contribution we found that for nearly half of the sources this component reaches the highest values outside the unresolved nucleus. We have interpreted this as most likely due to dust emission rather than scattered light from the accretion disc.

(iv) We found a correlation between the X-ray luminosity and HD, FC, and A_V . We attributed this correlation to the link they all have to the mass accretion rate on to the AGN: the AGN FC is produced by the accretion of gas, which is associated with more reddening; and it is also the source of heating for the circumnuclear dust, and thus increases the HD contribution.

(v) We also found an anticorrelation of HD, FC, A_V , and $\log(L_{\text{BoI,obs}})$ with xiy . We attribute it as a secondary effect, resulting from the fact that all of them are correlated, meaning that, when all their contributions increase, the result is a decreased contribution of the stellar population.

(vi) A correlation of $\log(L_{\text{BoI,obs}})$ with the mean age was also found. We attribute this correlation as due to the gas that is ejected by the intermediate-age population (at a 100 pc scale) during the stellar evolution phases being used to feed the AGN.

(vii) We also found that HD and FC components decrease outwards, xy and xyo increase from small to larger scales, while xiy , xio , and xo are nearly constant over the analysed region.

In general, our results show that there is a significant fraction of young stellar populations in the inner region of the active galaxies, suggesting that the inner region of these sources is facing a rejuvenation process with the AGN impacting on the recent star formation, in the sense that it can be associated with the decrease of young star formation towards the nuclear region.

ACKNOWLEDGEMENTS

We thank an anonymous referee for useful suggestions that helped to improve the paper. RR thanks to Conselho Nacional de Desen-

volvimento Científico e Tecnológico (CNPq, Proj. 311223/2020-6, 304927/2017-1, and 400352/2016-8), Fundação de Amparo à Pesquisa do Rio Grande do Sul (FAPERGS, Proj. 16/2551-0000251-7 and 19/1750-2), and Coordenação de Aperfeiçoamento de Pessoal de Nível Superior (CAPES, Proj. 0001). NZD acknowledges partial support from FONDECYT through project 3190769. CR acknowledges support from the FONDECYT Iniciacion grant 11190831 and ANID BASAL project FB210003. RAR acknowledges support from CNPq and FAPERGS. MB thanks to CAPES (Finance code 001).

This research is based on observations obtained at the Gemini Observatory, which is operated by the Association of Universities for Research in Astronomy, Inc., under a cooperative agreement with the NSF on behalf of the Gemini partnership: the National Science Foundation (USA), the Science and Technology Facilities Council (UK), the National Research Council Canada (Canada), CONICYT (Chile), the Australian Research Council (Australia), Ministério da Ciência e Tecnologia (Brazil), and south-east CYT (Argentina).

This research has made use of the NASA/IPAC Extragalactic Database (NED) that is operated by the Jet Propulsion Laboratory, California Institute of Technology, under contract with the National Aeronautics and Space Administration. We acknowledge the usage of the HyperLeda data base (<http://leda.univ-lyon1.fr>).

This research has made use of PHOTUTILS, an ASTROPY package for detection and photometry of astronomical sources (Bradley et al. 2019).

DATA AVAILABILITY

The NIFS data used in this paper are available in the Gemini Observatory Archive.⁶ They can also be shared by the first author under reasonable request.

REFERENCES

- Ajello M., Alexander D. M., Greiner J., Madejski G. M., Gehrels N., Burlon D., 2012, *ApJ*, 749, 21
- Alexander D. M., Hickox R. C., 2012, *New Astron. Rev.*, 56, 93
- Alonso-Herrero A. et al., 2019, *A&A*, 628, A65
- Alonso-Herrero A. et al., 2020, *A&A*, 639, A43
- Antonucci R., 1993, *ARA&A*, 31, 473
- Asari N. V., Cid Fernandes R., Stasińska G., Torres-Papaqui J. P., Mateus A., Sodré L., Schoenell W., Gomes J. M., 2007, *MNRAS*, 381, 263
- Astropy Collaboration et al., 2018, *AJ*, 156, 123
- Barbosa F. K. B., Storch-Bergmann T., Cid Fernandes R., Winge C., Schmitt H., 2009, *MNRAS*, 396, 2
- Barbosa F. K. B., Storch-Bergmann T., McGregor P., Vale T. B., Rogemar Riffel A., 2014, *MNRAS*, 445, 2353
- Barvainis R., 1987, *ApJ*, 320, 537
- Bewketu Belete A. et al., 2021, *A&A*, 654, A24
- Bianchin M. et al., 2022, *MNRAS*, 510, 639
- Bieri R., Dubois Y., Silk J., Mamon G. A., Gaibler V., 2016, *MNRAS*, 455, 4166
- Bradley L. et al., 2019, astropy/photutils: v0.6 (v0.6). Zenodo(<https://doi.org/10.5281/zenodo.2533376>)
- Burtscher L. et al., 2015, *A&A*, 578, A47
- Burtscher L. et al., 2021, *A&A*, 654, A132
- Caglar T. et al., 2020, *A&A*, 634, A114
- Cappellari M., 2017, *MNRAS*, 466, 798
- Cardamone C. N., Moran E. C., Kay L. E., 2007, *AJ*, 134, 1263
- Cardelli J. A., Clayton G. C., Mathis J. S., 1989, *ApJ*, 345, 245
- Cid Fernandes R., 2018, *MNRAS*, 480, 4480

⁶<https://archive.gemini.edu/searchform>

- Cid Fernandes R., Jr, Terlevich R., 1995, *MNRAS*, 272, 423
- Cid Fernandes R., Gu Q., Melnick J., Terlevich E., Terlevich R., Kunth D., Rodrigues Lacerda R., Joguet B., 2004, *MNRAS*, 355, 273
- Cid Fernandes R., Mateus A., Sodré L., Stasińska G., Gomes J. M., 2005, *MNRAS*, 358, 363
- Conroy C., 2013, *ARA&A*, 51, 393
- Crain R. A. et al., 2015, *MNRAS*, 450, 1937
- Croton D. J. et al., 2006, *MNRAS*, 365, 11
- Cuadra J., Nayakshin S., Springel V., Di Matteo T., 2006, *MNRAS*, 366, 358
- Dahmer-Hahn L. G. et al., 2019a, *MNRAS*, 482, 5211
- Dahmer-Hahn L. G. et al., 2019b, *MNRAS*, 489, 5653
- Dahmer-Hahn L. G. et al., 2022, *MNRAS*, 509, 4653
- Dametto N. Z. et al., 2019, *MNRAS*, 482, 4437
- Davies R. I., Sternberg A., Lehnert M. D., Tacconi-Garman L. E., 2005, *ApJ*, 633, 105
- Davies R. I., Müller Sánchez F., Genzel R., Tacconi L. J., Hicks E. K. S., Friedrich S., Sternberg A., 2007, *ApJ*, 671, 1388
- Davies R. I. et al., 2015, *ApJ*, 806, 127
- Davies R. I. et al., 2017, *MNRAS*, 466, 4917
- Davison A. C., Hinkley D. V., 1997, *Bootstrap Methods and Their Application*. Cambridge Univ. Press, Cambridge
- Dias B., Coelho P., Barbuy B., Kerber L., Idiart T., 2010, *A&A*, 520, A85
- Di Matteo T., Springel V., Hernquist L., 2005, *Nature*, 433, 604
- Diniz M. R., Riffel R. A., Storch-Bergmann T., Riffel R., 2019, *MNRAS*, 487, 3958
- Dottori H., Díaz R. J., Carranza G., Lípari S., Santos J., Jr, 2005, *ApJ*, 628, L85
- El-Badry K., Wetzell A., Geha M., Hopkins P. F., Kereš D., Chan T. K., Faucher-Giguère C.-A., 2016, *ApJ*, 820, 131
- Ellison S. L., Teimoorinia H., Rosario D. J., Mendel J. T., 2016, *MNRAS*, 458, L34
- Ellison S. L. et al., 2021, *MNRAS*, 505, L46
- Esquej P. et al., 2014, *ApJ*, 780, 86
- Fabian A. C., 2012, *ARA&A*, 50, 455
- Ferrarese L., Merritt D., 2000, *ApJ*, 539, L9
- Gallagher R., Maiolino R., Belfiore F., Drory N., Riffel R., Riffel R. A., 2019, *MNRAS*, 485, 3409
- Gao F. et al., 2020, *A&A*, 637, A94
- García-Burillo S. et al., 2019, *A&A*, 632, A61
- García-Burillo S. et al., 2021, *A&A*, 652, A98
- García-Rissmann A., Vega L. R., Asari N. V., Cid Fernandes R., Schmitt H., González Delgado R. M., Storch-Bergmann T., 2005, *MNRAS*, 359, 765
- Gaspar G., Díaz R. J., Mast D., D'Ambra A., Agüero M. P., Günthardt G., 2019, *AJ*, 157, 44
- Ge J., Yan R., Cappellari M., Mao S., Li H., Lu Y., 2018, *MNRAS*, 478, 2633
- Gebhardt K. et al., 2000, *ApJ*, 539, L13
- Goddard D. et al., 2017, *MNRAS*, 466, 4731
- Gomes J. M., Papaderos P., 2017, *A&A*, 603, A63
- Goulding A. D. et al., 2018, *PASJ*, 70, S37
- Granato G. L., Danese L., 1994, *MNRAS*, 268, 235
- Granato G. L., De Zotti G., Silva L., Bressan A., Danese L., 2004, *ApJ*, 600, 580
- Gratadour D., Rouan D., Mugnier L. M., Fusco T., Clénet Y., Gendron E., Lacombe F., 2006, *A&A*, 446, 813
- Greene J. E., Ho L. C., 2006, *ApJ*, 641, L21
- Harrison C. M., 2017, *Nat. Astron.*, 1, 1
- Heckman T. M., Best P. N., 2014, *ARA&A*, 52, 589
- Hennig M. G., Riffel R. A., Dors O. L., Riffel R., Storch-Bergmann T., Colina L., 2018, *MNRAS*, 477, 1086
- Hickox R. C., Mullaney J. R., Alexander D. M., Chen C.-T. J., Civano F. M., Goulding A. D., Hainline K. N., 2014, *ApJ*, 782, 9
- Hinshaw G. et al., 2013, *ApJS*, 208, 19
- Ho L. C., Greene J. E., Filippenko A. V., Sargent W. L. W., 2009, *ApJS*, 183, 1
- Hopkins P. F., 2012, *MNRAS*, 420, L8
- Hopkins P. F., Elvis M., 2010, *MNRAS*, 401, 7
- Ichikawa K., Ricci C., Ueda Y., Matsuoka K., Toba Y., Kawamuro T., Trakhtenbrot B., Koss M. J., 2017, *ApJ*, 835, 74
- Ishibashi W., Fabian A. C., 2012, *MNRAS*, 427, 2998
- Johnson B. D., Leja J., Conroy C., Speagle J. S., 2021, *ApJS*, 254, 22
- Kawakatu N., Wada K., 2008, *ApJ*, 681, 73
- Kennicutt R. C., Evans N. J., 2012, *ARA&A*, 50, 531
- King A., Pounds K., 2015, *ARA&A*, 53, 115
- Knapen J. H., Shlosman I., Peletier R. F., 2000, *ApJ*, 529, 93
- Koleva M., Prugniel P., Ocvirk P., Le Borgne D., Soubiran C., 2008, *MNRAS*, 385, 1998
- Koleva M., Prugniel P., Bouchard A., Wu Y., 2009, *A&A*, 501, 1269
- Kormendy J., Ho L. C., 2013, *ARA&A*, 51, 511
- Koski A. T., 1978, *ApJ*, 223, 56
- Koss M. et al., 2017, *ApJ*, 850, 74
- LaMassa S. M., Heckman T. M., Ptak A., Martins L., Wild V., Sonnentrucker P., Hornschemeier A., 2011, *ApJ*, 729, 52
- Lopes R. D. S., Storch-Bergmann T., Saraiva M. d. F., Martini P., 2007, *ApJ*, 655, 718
- Maccagni F. M., Morganti R., Oosterloo T. A., Mahony E. K., 2014, *A&A*, 571, A67
- McGregor P. J. et al., 2003, in Iye M., Moorwood A. F. M., eds, *Proc. SPIE Vol. 4841, Instrument Design and Performance for Optical/Infrared Ground-based Telescopes*. SPIE, Bellingham, p. 1581
- Madau P., Dickinson M., 2014, *ARA&A*, 52, 415
- Magorrian J. et al., 1998, *AJ*, 115, 2285
- Maiolino R. et al., 2017, *Nature*, 544, 202
- Mallmann N. D. et al., 2018, *MNRAS*, 478, 5491
- Maraston C., 2005, *MNRAS*, 362, 799
- Marian V. et al., 2020, *ApJ*, 904, 79
- Marshall M. A., Shabala S. S., Krause M. G. H., Pimblett K. A., Croton D. J., Owers M. S., 2018, *MNRAS*, 474, 3615
- Martins L. P., Riffel R., Rodríguez-Ardila A., Gruenwald R., de Souza R., 2010, *MNRAS*, 406, 2185
- Mason R. E. et al., 2015, *ApJS*, 217, 13
- Mauduit J.-C., Mamon G. A., 2007, *A&A*, 475, 169
- Nayakshin S., Zubovas K., 2012, *MNRAS*, 427, 372
- Novak G. S., Ostriker J. P., Ciotti L., 2011, *ApJ*, 737, 26
- Ocvirk P., Pichon C., Lançon A., Thiébaud E., 2006, *MNRAS*, 365, 46
- Oh K. et al., 2018, *ApJS*, 235, 4
- Oliva E., Origlia L., Maiolino R., Moorwood A. F. M., 1999, *A&A*, 350, 9
- Owen A., 2007, *Contemporary Math.*, 443, 59
- Pan H.-A. et al., 2019, *ApJ*, 881, 119
- Prieto M. A., Fernandez-Ontiveros J. A., Bruzual G., Burkert A., Schartmann M., Charlot S., 2019, *MNRAS*, 485, 3264
- Ramos-Almeida C. R., Ricci C., 2017, *Nat. Astron.*, 1, 679
- Rees M. J., 1989, *MNRAS*, 239, 1P
- Reichard T. A., Heckman T. M., Rudnick G., Brinchmann J., Kauffmann G., Wild V., 2009, *ApJ*, 691, 1005
- Ricci C., Ueda Y., Koss M. J., Trakhtenbrot B., Bauer F. E., Gandhi P., 2015, *ApJ*, 815, L13
- Ricci C. et al., 2017, *ApJS*, 233, 17
- Riffel R., Rodríguez-Ardila A., Pastoriza M. G., 2006, *A&A*, 457, 61
- Riffel R., Pastoriza M. G., Rodríguez-Ardila A., Maraston C., 2007, *ApJ*, 659, L103
- Riffel R., Pastoriza M. G., Rodríguez-Ardila A., Bonatto C., 2009, *MNRAS*, 400, 273
- Riffel R. A., Storch-Bergmann T., Riffel R., Pastoriza M. G., 2010, *ApJ*, 713, 469
- Riffel R., Ruschel-Dutra D., Pastoriza M. G., Rodríguez-Ardila A., Santos J. F. C., Jr, Bonatto C. J., Ducati J. R., 2011a, *MNRAS*, 410, 2714
- Riffel R., Bonatto C., Cid Fernandes R., Pastoriza M. G., Balbinot E., 2011b, *MNRAS*, 411, 1897
- Riffel R., Riffel R. A., Ferrari F., Storch-Bergmann T., 2011c, *MNRAS*, 416, 493
- Riffel R. A. et al., 2013a, *MNRAS*, 429, 2587
- Riffel R., Rodríguez-Ardila A., Aleman I., Brotherton M. S., Pastoriza M. G., Bonatto C., Dors O. L., 2013b, *MNRAS*, 430, 2002
- Riffel R. A., Vale T. B., Storch-Bergmann T., McGregor P. J., 2014, *MNRAS*, 442, 656
- Riffel R. et al., 2015, *MNRAS*, 450, 3069

- Riffel R. A. et al., 2016, *MNRAS*, 461, 4192
- Riffel R. A., Storchi-Bergmann T., Riffel R., Dahmer-Hahn L. G., Diniz M. R., Schönell A. J., Dametto N. Z., 2017, *MNRAS*, 470, 992
- Riffel R. A. et al., 2018, *MNRAS*, 474, 1373
- Riffel R. et al., 2019, *MNRAS*, 486, 3228
- Riffel R. et al., 2021a, *MNRAS*, 501, 4064
- Riffel R. A. et al., 2021b, *MNRAS*, 504, 3265
- Rodríguez-Ardila A., Pastoriza M. G., Viegas S., Sigut T. A. A., Pradhan A. K., 2004, *A&A*, 425, 457
- Rodríguez-Ardila A., Riffel R., Pastoriza M. G., 2005, *MNRAS*, 364, 1041
- Ruschel-Dutra D., Rodríguez Espinosa J. M., González Martín O., Pastoriza M., Riffel R., 2017, *MNRAS*, 466, 3353
- Rybicki G. B., Lightman A. P., 1979, *Radiative Processes in Astrophysics*. Wiley, New York
- Salaris M., Weiss A., Cassarà L. P., Piovan L., Chiosi C., 2014, *A&A*, 565, A9
- Sánchez S. F. et al., 2016, *Rev. Mex. Astron. Astrofis.*, 52, 21
- Sarzi M., Allard E. L., Knapen J. H., Mazzuca L. M., 2007, *MNRAS*, 380, 949
- Schawinski K., Koss M., Berney S., Sartori L. F., 2015, *MNRAS*, 451, 2517
- Schaye J. et al., 2015, *MNRAS*, 446, 521
- Schlegel D. J., Finkbeiner D. P., Davis M., 1998, *ApJ*, 500, 525
- Schönell A. J., Jr, Storchi-Bergmann T., Riffel R. A., Riffel R., 2017, *MNRAS*, 464, 1771
- Springel V. et al., 2005, *Nature*, 435, 629
- Storchi-Bergmann T., Schnorr-Müller A., 2019, *Nat. Astron.*, 3, 48
- Storchi-Bergmann T., González Delgado R. M., Schmitt H. R., Cid Fernandes R., Heckman T., 2001, *ApJ*, 559, 147
- Storchi-Bergmann T., McGregor P. J., Riffel R. A., Simões Lopes R., Beck T., Dopita M., 2009, *MNRAS*, 394, 1148
- Storchi-Bergmann T., Lopes R. D. S., McGregor P. J., Riffel R. A., Beck T., Martini P., 2010, *MNRAS*, 402, 819
- Storchi-Bergmann T., Riffel R. A., Riffel R., Diniz M. R., Borges Vale T., McGregor P. J., 2012, *ApJ*, 755, 87
- Terlevich E., Diaz A. I., Terlevich R., 1990, *MNRAS*, 242, 271
- Terrazas B. A. et al., 2020, *MNRAS*, 493, 1888
- Tody D., 1986, in Crawford D. L., ed., *Proc. SPIE Vol. 627, Instrumentation in Astronomy VI*. SPIE, Bellingham, p. 733
- Tody D., 1993, in Hanisch R. J., Brissenden R. J. V., Barnes J., eds, *ASP Conf. Ser. Vol. 52, Astronomical Data Analysis Software and Systems II*. Astron. Soc. Pac., San Francisco, p. 173
- Tojeiro R., Heavens A. F., Jimenez R., Panter B., 2007, *MNRAS*, 381, 1252
- Trussler J., Maiolino R., Maraston C., Peng Y., Thomas D., Goddard D., Lian J., 2020, *MNRAS*, 491, 5406
- Villforth C. et al., 2014, *MNRAS*, 439, 3342
- Vogelsberger M. et al., 2014, *Nature*, 509, 177
- Walcher J., Groves B., Budavári T., Dale D., 2011, *Ap&SS*, 331, 1
- Wang X., Loeb A., 2018, *New Astron.*, 61, 95
- Waskom M. L., 2021, *J. Open Source Softw.*, 6, 3021
- Wilkinson D. M., Maraston C., Goddard D., Thomas D., Parikh T., 2017, *MNRAS*, 472, 4297
- Worthey G., Faber S. M., Gonzalez J. J., Burstein D., 1994, *ApJS*, 94, 687
- Yang Q.-X., Xie F.-G., Yuan F., Zdziarski A. A., Gierliński M., Ho L. C., Yu Z., 2015, *MNRAS*, 447, 1692
- Zubovas K., Bourne M. A., 2017, *MNRAS*, 468, 4956
- Zubovas K., Nayakshin S., King A., Wilkinson M., 2013, *MNRAS*, 433, 3079

SUPPORTING INFORMATION

Supplementary data are available at *MNRAS* online.

- Figure S1.** The same as Fig. 3, but for NGC 788.
- Figure S2.** The same as Fig. 3, but for NGC 1052.
- Figure S3.** The same as Fig. 3, but for Mrk 79.
- Figure S4.** The same as Fig. 3, but for NGC 1125.
- Figure S5.** The same as Fig. 3, but for NGC 1068.
- Figure S6.** The same as Fig. 3, but for NGC 2110.
- Figure S7.** The same as Fig. 3, but for NGC 3227.
- Figure S8.** The same as Fig. 3 but for NGC 3516.
- Figure S9.** The same as Fig. 3, but for NGC 4235.
- Figure S10.** The same as Fig. 3, but for NGC 5506.
- Figure S11.** The same as Fig. 3, but for NGC 5548.
- Figure S12.** The same as Fig. 3, but for NGC 5899.
- Figure S13.** The same as Fig. 3, but for NGC 5929.
- Figure S14.** The same as Fig. 3, but for Mrk 607.
- Figure S15.** The same as Fig. 3, but for Mrk 766.
- Figure S16.** The same as Fig. 3, but for Mrk 1066.
- Figure S17.** The same as Fig. 3, but for Mrk 1157.

Please note: Oxford University Press is not responsible for the content or functionality of any supporting materials supplied by the authors. Any queries (other than missing material) should be directed to the corresponding author for the article.

This paper has been typeset from a $\text{\TeX}/\text{\LaTeX}$ file prepared by the author.